AFRL-RY-HS-TR-2011-0010

ELECTROMAGNETIC PROPERTIES OF MATERIALS AND METAMATERIALS

John S. Derov, Alvin D. Drehman, Everett E. Crisman, Beverly Turchinetz, Drayton Hanna, and Steve Best

20 September 2010

Final Report

AIR FORCE RESEARCH LABORATORY
Sensors Directorate
Electromagnetics Technology Division
80 Scott Drive
Hanscom AFB MA 01731-2909

NOTICE AND SIGNATURE PAGE

Using Government drawings, specifications, or other data included in this document for any
purpose other than Government procurement does not in any way obligate the U.S. Government.
The fact that the Government formulated or supplied the drawings, specifications, or other data
does not license the holder or any other person or corporation; or convey any rights or
permission to manufacture, use, or sell any patented invention that may relate to them.

This report was cleared for public release by the Electronic Systems Center Public Affairs Office
for the Air Force Research Laboratory Electromagnetic Technology Division and is available to
the general public, including foreign nationals. Copies may be obtained from the Defense
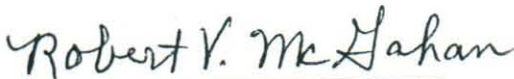Technical Information Center (DTIC) (http://www.dtic.mil).

AFRL-RY-HS-TR-2011-0010 HAS BEEN REVIEWED AND IS APPROVED FOR PUBLIC
RELEASE.

JOHN S. DEROV
Program Manager
Antenna Technology Branch

DAVID CURTIS
Branch Chief
Antenna Technology Branch

ROBERT V. MCGAHAN
Technical Communications Advisor
Electromagnetics Technology Division

This report is published in the interest of scientific and technical information exchange, and its
publication does not constitute the Government's approval or disapproval of its ideas or findings.

REPORT DOCUMENTATION PAGE		Form Approved OMB No. 0704-0188

Public reporting burden for this collection of information is estimated to average 1 hour per response, including the time for reviewing instructions, searching existing data sources, gathering and maintaining the data needed, and completing and reviewing this collection of information. Send comments regarding this burden estimate or any other aspect of this collection of information, including suggestions for reducing this burden to Department of Defense, Washington Headquarters Services, Directorate for Information Operations and Reports (0704-0188), 1215 Jefferson Davis Highway, Suite 1204, Arlington, VA 22202-4302. Respondents should be aware that notwithstanding any other provision of law, no person shall be subject to any penalty for failing to comply with a collection of information if it does not display a currently valid OMB control number. PLEASE DO NOT RETURN YOUR FORM TO THE ABOVE ADDRESS.

1. REPORT DATE (DD-MM-YYYY) 06-09-2010	2. REPORT TYPE FINAL REPORT	3. DATES COVERED (From - To) 01 NOV 2001 – 30 Sept 2009
4. TITLE AND SUBTITLE "Electromagnetic Properties of Materials and Metamaterials"		5a. CONTRACT NUMBER In-house
		5b. GRANT NUMBER
6. AUTHOR(S) John S. Derov*, Alvin D. Drehman*, Everett E. Crisman**, Beverly Turchinetz***, Drayton Hanna****, and Steve Best****		5d. PROJECT NUMBER 2305
		5e. TASK NUMBER HA
		5f. WORK UNIT NUMBER 02

7. PERFORMING ORGANIZATION NAME(S) AND ADDRESS(ES)

*AFRL/RYHA
80 Scott Dr.
Hanscom AFB, MA 01731-2909

** University of Rhode Island
Chem. Eng. Crawford Hall
Kingston, RI 02881

*** Photonics Inc.
900 Middlesex Turnpike Bldg 5
Billerica, MA 01821

**** MITRE Corp.
202 Burlington Rd.
Bedford, MA 01730

8. PERFORMING ORGANIZATION REPORT

9. SPONSORING / MONITORING AGENCY NAME(S) AND ADDRESS(ES) Electromagnetics Technology Division AFOSR Air Force Research Laboratory 80 Scott Drive Hanscom AFB MA 01731-2909	10. SPONSOR/MONITOR'S ACRONYM(S) AFRL/RYHA
	11. SPONSOR/MONITOR'S REPORT AFRL-RY-HS-TR-2011-0010

12. DISTRIBUTION / AVAILABILITY STATEMENT
DISTRIBUTION APPROVED FOR PUBLIC RELEASE
66ABW-2011-0399.

13. SUPPLEMENTARY NOTES

14. ABSTRACT This research encompassed three areas of study the nonlinear behavior of high temperature superconductors (HTS) and a micro-electro-mechanical HTS switch, left-handed or negative index metamaterials, and surface plasmon behaviour in nanoparticle media. The study focused on the electromagnetic properties materials for devices and components at microwave frequencies.

15. SUBJECT TERMS
High temperature superconductors, MEMS, negative refractive index, left-handed materials, Double negative, metamaterials, plasmonics

16. SECURITY CLASSIFICATION OF:			17.LIMITATION OF ABSTRACT	18.NUMBER OF PAGES	19a. NAME OF RESPONSIBLE PERSON John S. Derov
a. REPORT Unclassified	b. ABSTRACT Unclassified	c.THIS PAGE Unclassified	UU	47	19b. TELEPHONE NUMBER (include area code) 781-377-2638

Standard Form 298 (Rev. 8-98)
Prescribed by ANSI Std. Z39.18

ii

TABLE OF CONTENTS

TABLE OF FIGURES

ACRONYMS

AES.............................Auger Electron Spectroscopy
AFM............................Atomic Force Microscopy
$BaTiO_3$........................Barium Titinate
CPW............................co-planer waveguide
DARPA........................Defense Advance Research Agency
DC.............................direct current
DNG..........................double-negative
E................................electric
E-field....................electric field
ESCA.........................electron-spectroscopy-for-chemical-analysis
EVM...........................Error Vector Magnitude
GHz............................Giga-Hertz
H................................magnetic
H-field.................magnetic-field
HPBW........................half power bandwidth
HTS ....High Temperature Superconductor
IMD............................intermodulation distortion
LHM...........................left-handed-material
MEM...........................micro-Machined-Electrico-Mechanical
NIM............................negative index metamaterial
NRI.............................negative refractive index
PCboards....................printed circuit boards
QPSK..........................Quadrature Phase Shift Keying
Rx...............................receive
Si_3N_4..........................Silicon Nitride
SRR............................split-ring-resonator
Tc...............................critical temperature
TE..............................transverse electric
TEM...........................transverse electromagnetic
TM.............................transverse magnetic
Tx...............................transmit
w. r. t. ....with respect to
XeF_2 ....Xenon difluorider
XPS...........................X-ray-photoelectron spectroscopy
YBCO ....Yttrium Barium Copper Oxide
ZIM............................zero index medium

ABSTRACT

This research encompassed three areas of study: i) high temperature superconductivity, ii) left-handed materials or negative index materials, and iii) surface plasmons. The study focused on the electromagnetic of properties materials for devices and components at microwave frequencies.

Starting with high temperature superconductivity (HTS), the HTS research task studied two topics: i) the non-linear behavior of Yttrium Barium Copper Oxide (YBCO) and ii) the fabrication and characterization of a HTS micro-machined-electro-mechanical (MEM) switch. The existing HTS materials exhibit a non-linear behavior in the microwave frequency range as a function of power. Measurements were to understand and control the nonlinear behavior of YBCO and to improve its power handling capability. A means to achieve this was to dope the YBCO with Ca. The results of the study indeed showed the nonlinear microwave properties of YBCO could be suppressed by using Ca as a dopent. The HTS MEM switch was studied to provide a low loss switch that was compatible with low power HTS YBCO filters. One of the fabrication problems was the use of silicon nitride isolation layer between the actuator and the YBCO transmission of the switch and the xenon-difluoride (XeF_2) etchant used to release the actuator. Our study showed that XeF_2 affected the superconducting properties of the YBCO. The solution was the use of a thin gold capping layer over the YBCO to act as a diffusion barrier to reduce the reaction between the silicon nitride and XeF_2 with the YBCO.

The second area of research, left-handed or negative index metamaterials, was established after the demonstrations of a propagation of a plane wave through a medium with simultaneously negative permeability and permittivity or a medium with a negative refractive index. The research is based on a medium using split-ring-resonators (SRRs) and wire-posts to generate the medium's simultaneous negative permeability and permittivity. The SRR-wire-posts medium is similar to the medium used in the first demonstration of a negative refraction. In this study we demonstrated that the SRR-wire-post medium does obey Snell's law, has a bi-anisotropic behavior, and has radiative and ohmic losses. The study shows that bi-anisotropy makes the medium polarization sensitive.

The plasmon research task is in its initial stages of studying nano-particle structures that mimic electric and magnetic plasmon behavior. The electric plasmon behavior exhibits negative permittivity and the magnetic plasmon behavior exhibits negative permeability. The goal of the research is to study the plasmonic behavior of the nano-particles and control the plasmonic behavior for the development of electro-optical components and devices for various applications including beam-steering

1.0 MICROWAVE BEHAVIOR OF HIGH TEMPERATURE SUPERCONDUCTORS AND MEM DEVICE

1.1 Introduction

High-temperature superconductors (HTS), discovered in the mid-1980s, have a transition between its normal and superconducting state at a critical temperature (T_c) above 20°K. Karl Muller and George Bednorz discovered the first high-temperature superconductor[1] and published their findings in 1986. Their paper reported on a cuprate-based ceramic with a superconducting critical temperature of T_c = 35°K. Thereafter, the cuprate-based ceramics were studied extensively resulting in the discovery of ceramics with even higher T_c's. The most widely used HTS's are Bismuth Strontium Calcium Copper Oxide and Yttrium Barium Copper Oxide[2,3], (YBCO), both of which have T_c above that of liquid nitrogen (77°K). When HTS materials became available with T_c's above 77°K, they became economical for use in certain RF applications. Satellite and ground station communications links, for example, were fitted with high efficiency HTS filters, which significantly improved the performance of the receivers while reducing their mass by 45%. The increased interest in HTS for RF applications, lead to RF transmitter applications. However, during the study of the high-power application, HTS materials were observed to exhibited deleterious nonlinear behavior when very high RF power was applied.

1.2 Non-linear Superconducting Microwave Properties in YBCO

The nonlinear behavior of HTS thin films limited their use at microwave frequencies. Specifically thin films of HTS generated inter-modulation distortion (IMD) in filters[4]. The nonlinear behavior in the HTS films is a result of the current-induced critical state[5], which causes the HTS to return to the normal conductivity state. The super/normal transition is dependent on the current density of the superconductor where j_c is often referred to as the critical current density. In the superconducting state the magnetic field produced by the current generates fluxons. As the current in the HTS is increased the fluxon density increases and nonlinear behavior is observed at the j_c threshold. To some extent the fluxon density can be controlled by doping the HTS with fluxon "pining" sites thereby increasing the j_c threshold.

To determine whether the high frequency losses and nonlinearities could be reduced by using the fluxon pining concept we used calcium (Ca) as the dopant. The diffusion of Ca into HTS material had previously been shown increase j_c at dc and low frequency power distributions[6]. To study the effect of Ca on the j_c of HTS films at high frequencies, HTS films were doped with Ca as described below. It was observed that the Ca atoms were collecting along the grain-boundaries in the film and implied that the pining of the fluxons was among those boundaries as well.
In our study epitaxial YBCO films were grown on both lanthanum aluminate and magnesium oxide substrates. The Ca doping was achieved by depositing a surface layer from a sputter target (ratio 70/30 atomic percent, Y/Ca) on top of epitaxial YBCO films. The thicknesses of the surface Y/Ca layers were nominally 20nm and 40nm. An improvement in the linear microwave surface resistance R_s was observed for the HTS films with the 20nm thick surface layer. The linear and nonlinear microwave properties of the HTS films with the 40nm thick surface layer were degraded. We concluded that the larger amount of Ca available in the 40nm films allowed Ca substitution at the Ba sites in the crystal structure instead of just at the grain-boundaries[7].

1.3 Superconducting MEM switch

Despite the high frequency nonlinearity problems of HTS films, they are still quite useful for use as narrow band microwave filters. To make them functional as filters, one needs to match the filter to the frequency of interest and this requires an appropriate microwave switch. Ideally, the switches should operate at cryogenic temperatures to minimize their losses. To accomplish this we developed a micro-machined-electro-mechanical (MEM) HTS switch. A schematic of MEM switch design is shown in Figure 1. The three salient components of the HTS-MEM switching are: 1) the coplanar waveguide (CPW) transmission line, 2) the bimetal actuator membrane and 3) the capacitor formed by the dielectric layer between the actuator and CPW transmission.
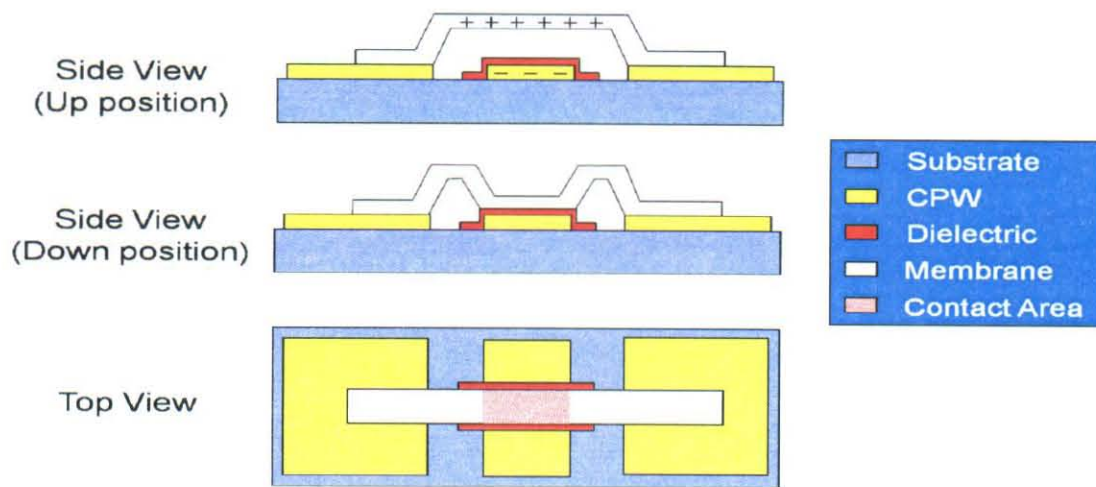
Figure 1: Schematic of HTS-MEM switch

Since little was known about a HTS-MEM switch, our research initiative covered both the electrical and the mechanical properties of the switch at low temperature as well as the material aspects of engineering a HTS-MEM switch.

1.4 MEM Switch Material Study

The material properties related to developing a HTS-MEM switch were extensively evaluated w.r.t. the effect of the fabrication steps. Fabrication of the switch involved a six step process;
1) growing YBCO film on a lanthanum aluminate substrate,
2) depositing and patterning a coplanar waveguide transmission line in the HTS film,
3) depositing and patterning a dielectric layer,
4) depositing and patterning a silicon sacrificial layer,
5) depositing and patterning a bimetal actuator for the switch, and
6) releasing the actuator by removing the silicon sacrificial layer in a dry etching process.

Steps 1 and 2 of the fabrication process, the HTS film growth and patterning for the coplanar waveguide, were well understood before the start of the program. The remaining four steps of fabrication required that the superconducting behavior of the HTS film to be evaluated after each step. The deposition of the dielectric capacitive layer was the first concern. The most common capacitive layer used in fabricating standard MEM switches is silicon nitride (Si_3N_4). Silicon nitride

has the highest breakdown voltage of commonly available microelectronic materials but, the presence of Si in HTS films is known to deteriorate their superconducting properties. Two dielectric materials were chosen for evaluation: Si_3N_4 for its high breakdown voltage and barium titanate ($BaTiO_3$) for its compatibility with YBCO. The Si_3N_4 layers were deposited by reactive sputtering using 50/50 partial pressure mixture of argon and nitrogen. For the $BaTiO_3$, a 50/50 mixture of oxygen and argon was used. The dielectrics were deposited over the center conductor of two different CPW patterns and then the DC resistances of the conductors were measured to compare with the pre-sputter-coated values. Figure 2 shows the resistance of the patterned YBCO film compared with the resistances after the dielectric depositions. It is evident in the figure that both silicon nitride and barium titanate degrade the superconducting property of the HTS film to some extent. However, it is also clear that the Si_3N_4 effect is much more pronounced than that of $BaTiO_3$.
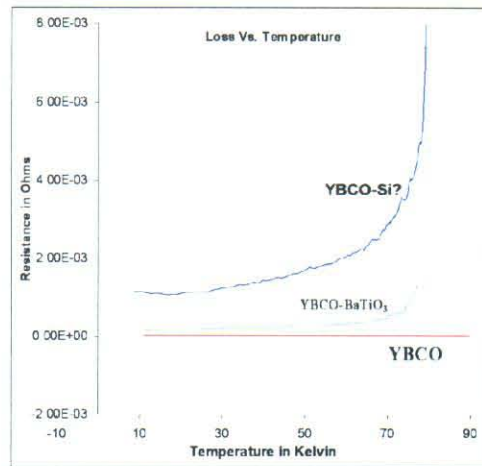
Figure 2: Temperature dependence of the DC resistance of YBCO-HTS films before and after the deposition of the Si3N4 and BaTiO3 dielectric layers.

To understand the effect the Si_3N_4 and $BaTiO_3$ has on the HTS material x-ray photoelectron spectroscopy (XPS or ESCA) profiling of the dielectric/YBCO interface was performed. The XPS profiling technique is a destructive measurement. Material is sputtered away in minute steps and the XPS signatures of the successively exposed surfaces are recorded after each step. The result is a trace of the chemical composition through the dielectric thin film, through the interface, and into the HTS beneath. This allowed us to determine if components of either the SiN_4 or the $BaTiO_3$ have migrated into their respective HTS layers. Silicon, reacting with oxygen in the YBCO, has the highest probability of diffusing. Since the superconducting property of YBCO is related to the meta-stable oxygen ratio, too much or too little oxygen will extinguish the superconducting property of the HTS film.

4
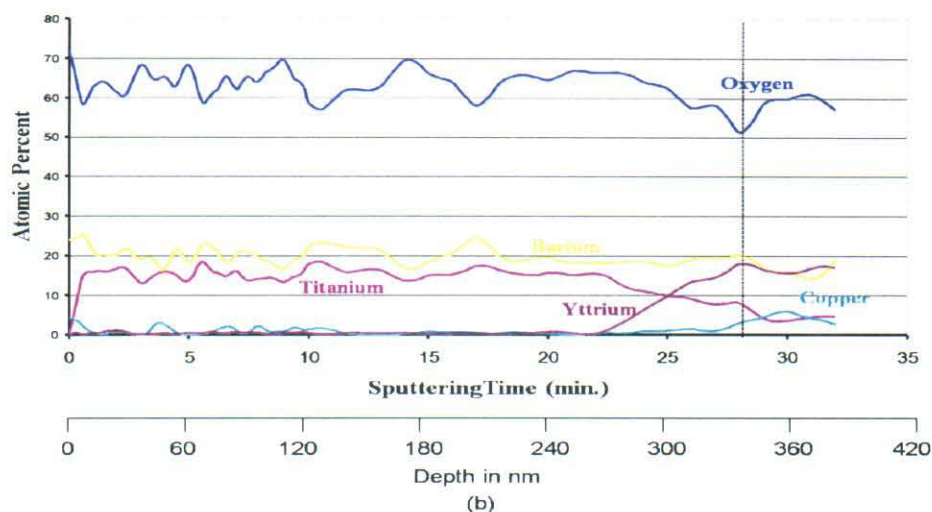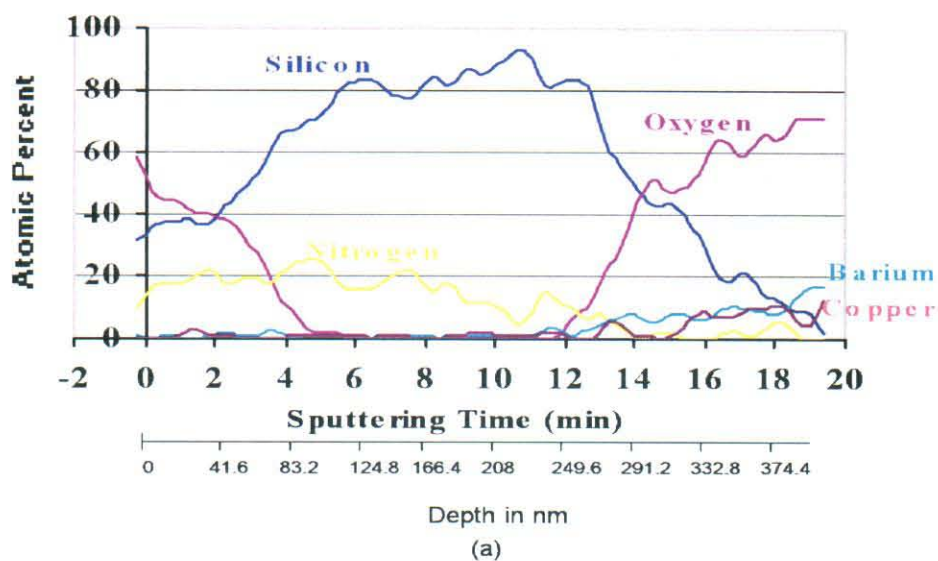
Figure 3: XPS profiles of (a) an approximately 350 nm thick SiN4 film on YBCO and (b) of approximately 350 nm BaTiO3 film on YBCO

Figure 3(a) and 3(b) shows the atomic percent of the elements present in the material as the sampled surface progresses through material. In figure 3(a) the first 80nm or so is the surface of the Si_3N_4 film which has clearly reacted with the ambient oxygen. As X-ray probe moves further through the film the dominant elements are silicon and nitrogen from the SiN_4. Between 250nm and 370nm the interface between the Si_3N_4 and YBCO is reached. Since the Si signal extends into the YBCO regime, the indication is that Si has diffused well into the HTS and is the likely cause of the degradation of the superconducting properties seen (for the Si_3N_4/YBCO specimen) in figure 2. Thus Si_3N_4 cannot be used directly on the YBCO-HTS. Figure 3(b) shows the results for the YBCO with the $BaTiO_3$ layer. As anticipated the surface of the $BaTiO_3$ has greater stability and does not appear to be affected by exposure to air. As the XPS X-ray beam samples further into the film the dominant elements become oxygen, barium, and titanium until the depth is approximately 300nm where yttrium starts to be observed and the titanium signal decreases. At approximately

350nm Cu starts to be observed and the Ti line is approaching zero atomic percent. This occurs approximately at the interface for BaTiO$_3$ with YBCO. Though some inter-diffusion has occurred, the oxygen level of the YBCO appears to be unaffected. Comparing Si$_3$N$_4$ and the BaTiO$_3$ less Ti appears too diffused into the YBCO relative to and so the HTS degradation is reduced by using BaTiO$_3$ instead of Si$_3$N$_4$.

The final part of the switch fabrication process involves 'releasing' the switch actuator layer. For this step we use xenon-difluoride to etch away the silicon sacrificial layer. No information about chemistry between XeF$_2$ and YBCO was available so, experiments were performed to determine whether the XeF$_2$ treatment would deteriorate the properties of the HTS films. To study the interaction a series of XeF$_2$ etching experiments were performed and evaluated using an atomic force microscopy (AFM) and XPS. Separate films were grown in the crystallographic c- and a-axes directions to determine if etching proceeded in a preferred direction. The AFM results for the c-axis oriented film[8,9] are shown in figure 4.

Image Statistics	
Img. Z range	36.132 nm
Img. Mean	0.021 nm
Img. Raw mean	-44.457 nm
Img. Rms (Rq)	3.096 nm
Img. Ra	2.131 nm

Image Statistics	
Img. Z range	22.936 nm
Img. Mean	0.018 nm
Img. Raw mean	-3.014 nm
Img. Rms (Rq)	2.901 nm
Img. Ra	2.318 nm
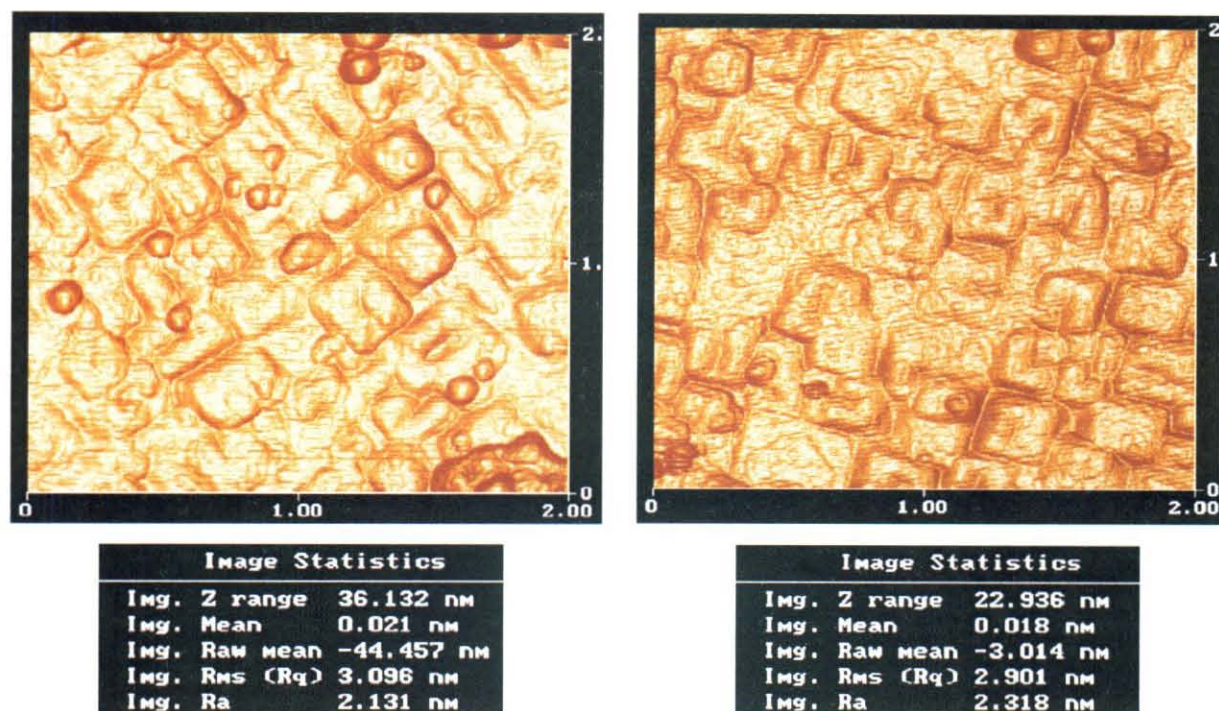
Figure 4: YBCO c-axis AFM micrographs showing; (a) the surface of the YBCO film before XeF$_2$ etching. The surface shows the screw dislocations typical of c-axis YBCO film growth. (b) the surface of the film after XeF$_2$ etching. From these micrographs it is evident that the XeF$_2$ etch cycle has minimal effect on the YBCO c-axis.

The main difference in the two micrographs is the surface roughness of the film. After etching the film showed a 36% decrease in the peak-to-peak values of the roughness and a 6% decrease in the rms value of the surface roughness. Similar AFM micrographs and statistics for a-c axes film growth are shown in Figure 5 where (a) is the surface before etching and (b) the surface after etching. Note that the figure 5 micrograph for the a-c axes film in (a) shows a mottled film surface, which was removed in seconds when exposed to the XeF$_2$. After etching, seen in micrograph (b), the "lattice weave" characteristic of a-c axes film growth[10] was observed. The surface roughness

for the a-c axes film increased after etching 51% for the peak-peak roughness and 14% for the rms roughness. The etching properties of c and a-c axes YBCO films are different, but the etching properties do not seem to be related to the crystallographic orientation of the films.

Image Statistics	
Img. Z range	104.47 nm
Img. Mean	0.123 nm
Img. Raw mean	16.935 nm
Img. Rms (Rq)	10.857 nm
Img. Ra	5.959 nm

Image Statistics	
Img. Z range	159.77 nm
Img. Mean	0.022 nm
Img. Raw mean	-14.701 nm
Img. Rms (Rq)	12.399 nm
Img. Ra	7.122 nm
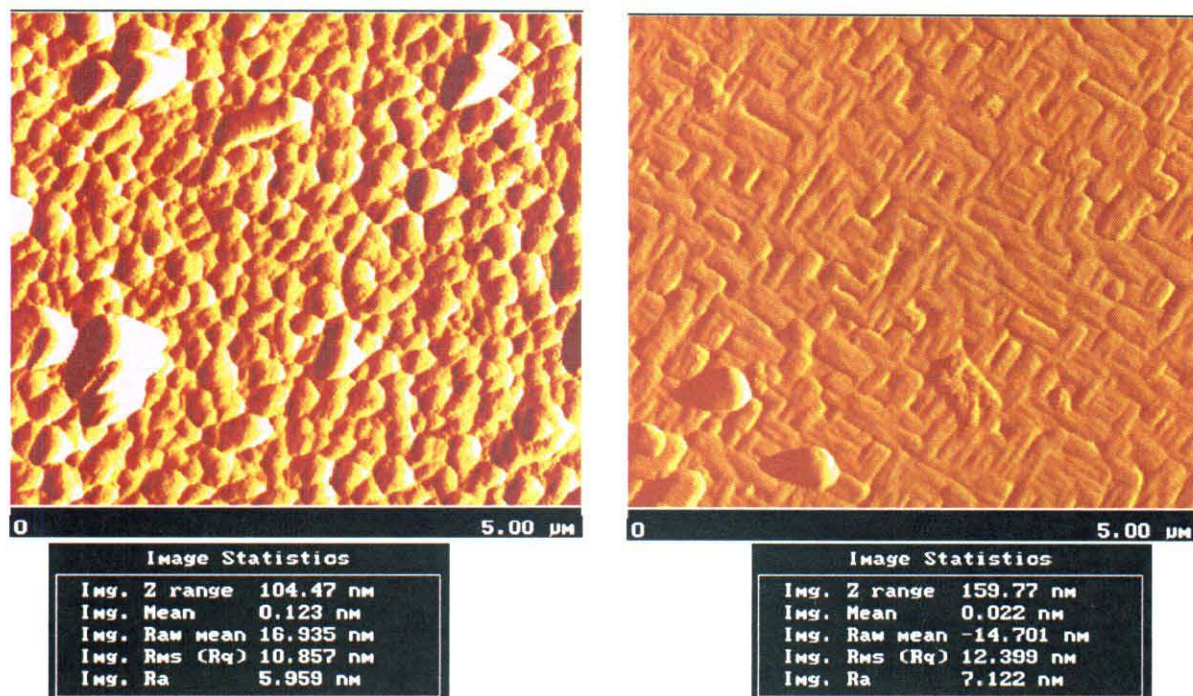
To determine if the fluorine reacted with the YBCO, changes in the binding energy for the

Figure 5: (a) AFM micrograph for an a-c axes YBCO film shows the mottled surface of the before XeF$_2$ etching and (b) after etching shows the lattice weave structure typical of a-c axes film growth for YBCO.

elements in the film were evaluated using XPS. The XPS profiles were performed on the un-etched and etched films and the results for a typical set of films are shown in Figure 6(a) and (b). In that figure one can see the composition of the film before and after etching respectively. Figure 6(a) the film before etching shows no trace of fluorine, but in 6(b) the film, after etching, does show evidence of fluorine.

(a)

(b)
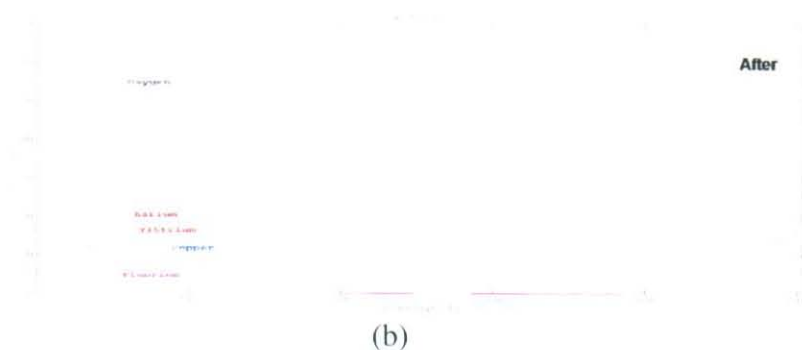
Figure 6: XPS composition of YBCO before and after XeF$_2$ etching (a) shows no fluorine in the film and (b) shows that fluorine is present in the surface after etching.
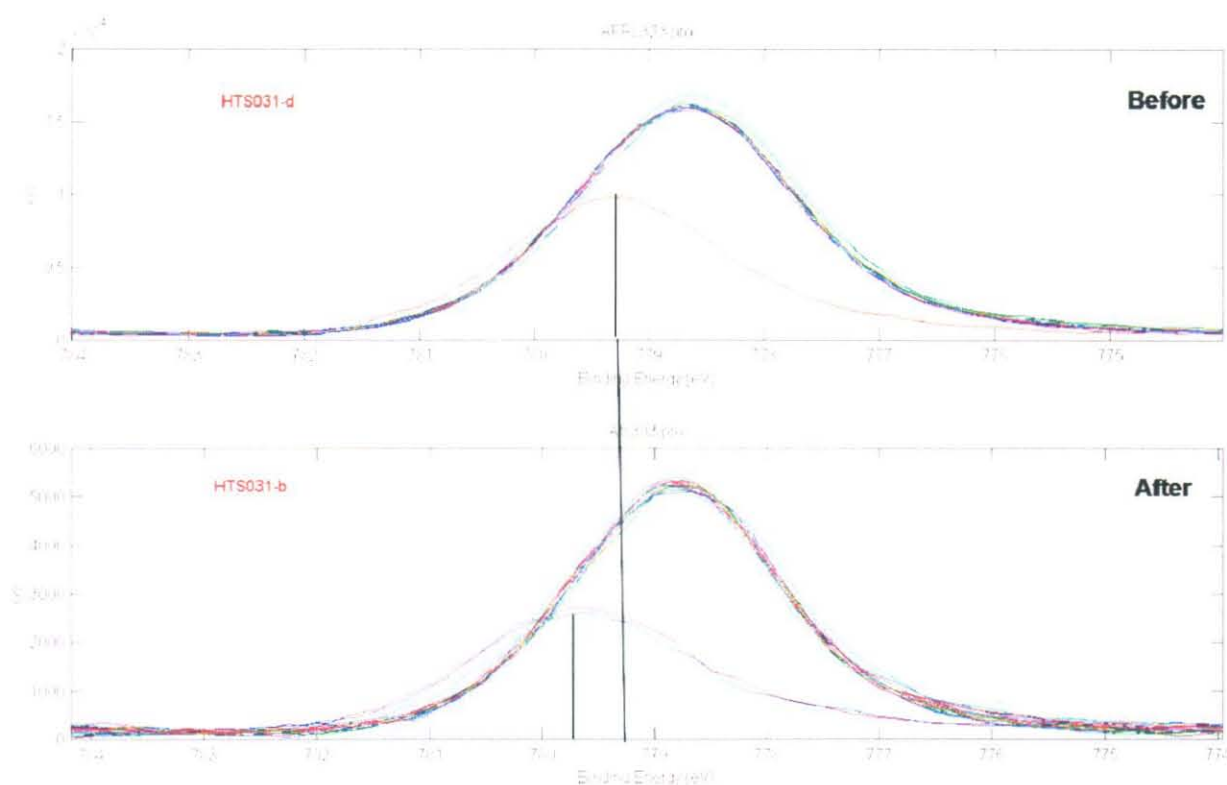
Figure 7: XPS binding energy for YBCO film; (a) before XeF$_2$ etching and (b) after etching. A 0.29 eV shift in the Ba binding energy is seen from (a) to (b).

Figure 7 (a) and (b) shows the binding energy for the elements in the YBCO before and after etching with XeF$_2$. A change in binding energy for Ba can be seen by comparing (a) and (b). In (a) the bond for Ba increases in energy starting from the interior of the film at 778.65 eV moving toward the surface at 779.36 eV. In (b) the bond energy for Ba increases by 0.29 eV at the surface for the film after XeF$_2$ etching. Our conclusion at this point in our investigation is that XeF$_2$ both etches the surface of YBCO and interacts with the barium in that surface. The XPS measurements indicate that fluorine reacts with the Ba in the YBCO film.

8

Using a constant current source, the temperature dependence of voltage drop across the HTS film was measured for the YBCO film before and after etching (figure 8). Though the T_c after etching was the same as the Tc before etching, the film's normal resistance was significantly increased by the etching process.
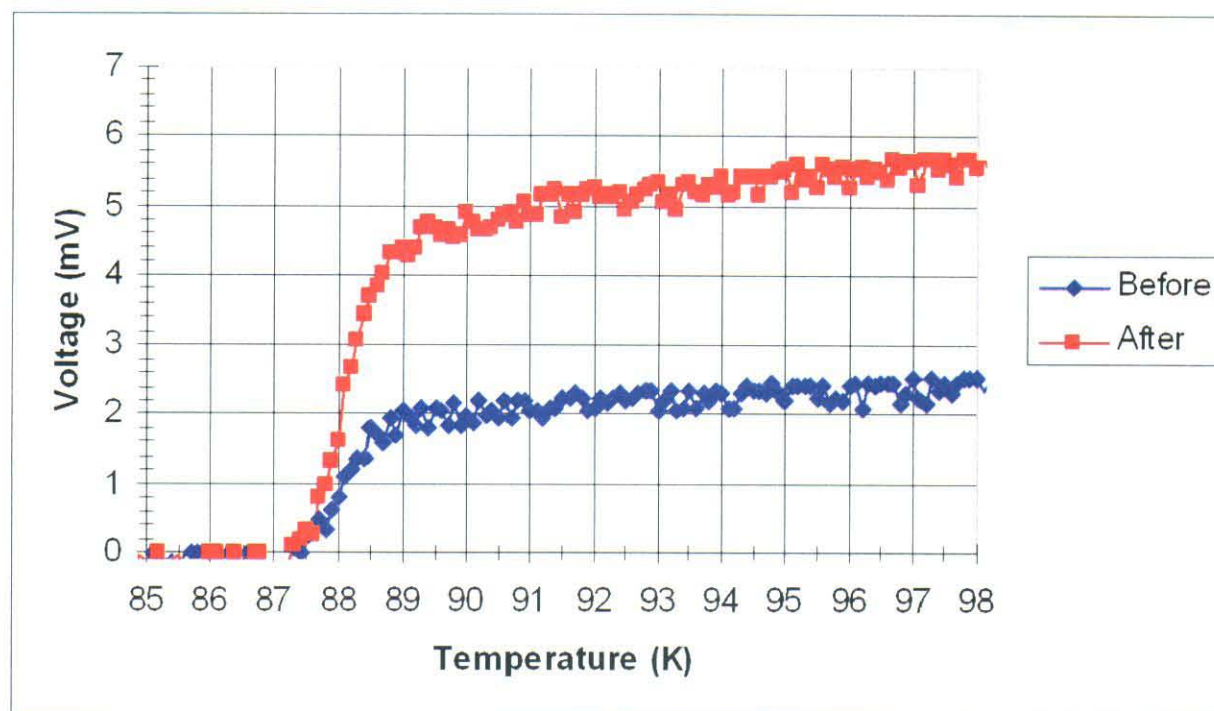
Figure 8: T_c measurements before and after XeF_2 etching of a YBCO film

The results of the material study showed that the SiN_4, $BaTiO_3$, and XeF_2 processing both significantly affected the properties of YBCO films[11]. To eliminate these interactions a thin layer (~ 30 nm) of gold (Au) was used as a diffusion barrier between the Si_3N_4, $BaTiO_3$, and YBCO film.

Conclusions: From the measurements presented above we conclude that xenon-difluoride processing etches YBCO and that the kinetics of the reaction is slow (~1.1Å/s). Both a-axis and mixed a/c–axis orientation react with XeF_2 and the mottled surface sometimes found on YBCO thin films has a greater etch rate, although no quantitative value for that was established. The Auger electron spectroscopy (AES) results[11], not shown here, show that the XeF_2 process etches the superconducting composition of YBCO compounds faster than the copper rich compound implying that fluorine reacts with specific components of YBCO. The XPS analysis shows fluorine to a depth of 40nm with barium as the only component showing measurable chemical bond shifting. This implies that BaF_2 is probably the compound that facilitates the fluorine progression into the film surface. Finally, the etch process does not affect the superconducting transition temperature of the film, but does change the sheet resistance somewhat.

1.5 MEM SWITCH Mechanical Properties

Beside the material science studies necessary for fabricating the HTS MEM switch, the mechanical properties of the HTS switch structure must be known, as a function of temperature. A first order

model describing the mechanical behavior of the switch based on the pressure balance model[12] is summarized below with reference to the schematic of Figure 9. In the schematic, a membrane actuator, represented by the upper plate of a parallel capacitor, is suspended by a spring. The pressure P_R is related to the restoring force of the spring, K_S is the spring constant, P_{ES} is the pressure due to the actuating electrostatic potential, and V is voltage source that produces the electrostatic potential. Then the equations of motion for the pressure balance model are given by equations below. P_R is given in equation (1.5.1) where g_0 is the initial (un-actuated) distance between the capacitor plates for V = 0, and g is the thickness of dielectric, then equation (1.5.2) can be used to relate K_S to the physical properties of the membrane; E the Young's modulus, t the thickness of the beam, L the length of the beam, and σ the Poisson's ratio. Equation (1.5.3) then relates the electrostatic pressure, P_{ES}, between the parallel plates a distance g apart, to the applied voltage, V, with ε_0 as the free space permittivity.
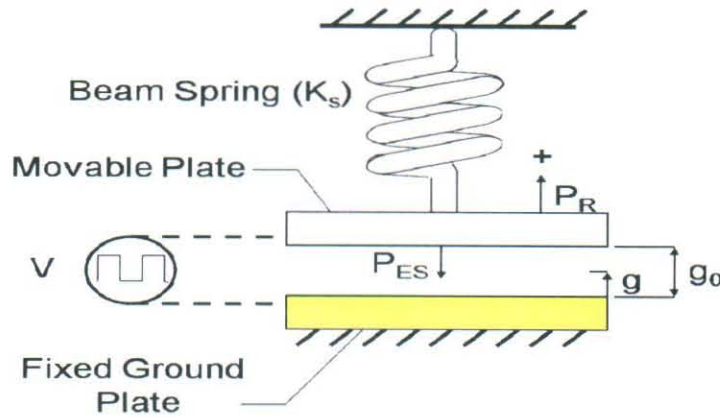
Membrane Displacement $\Rightarrow$ $P(g) = P_R + P_{ES}$

Static Equilibrium $\Rightarrow$ $P(g) = 0$

Figure 9: Schematic for pressure balance model equation of motion

$$P_R = K_s(g_0 - g) \qquad \text{eq.(1.5.1)}$$

$$K_s = \frac{32Et^3}{L^4} + \frac{8\sigma(1-\gamma)t}{L^2} \qquad \text{eq.(1.5.2)}$$

$$P_{es} = -\frac{\varepsilon_0 V^2}{2g^2} \qquad \text{eq.(1.5.3)}$$

$$V = \sqrt{\frac{8g_0^3}{27\varepsilon}\left(\frac{32Et^3}{L^4} + \frac{8\sigma(1-\gamma)t}{L^2}\right)} \qquad \text{eq.(1.5.4)}$$

The pull-down voltage for a normal conducting switch increases as membrane thickness increases as shown in Figure 10. The relationship between the pull-down voltage and the membrane mechanical properties is given in equation (1.5.4) where ε is the effective permittivity of the dielectric region between the membrane and transmission line.

10
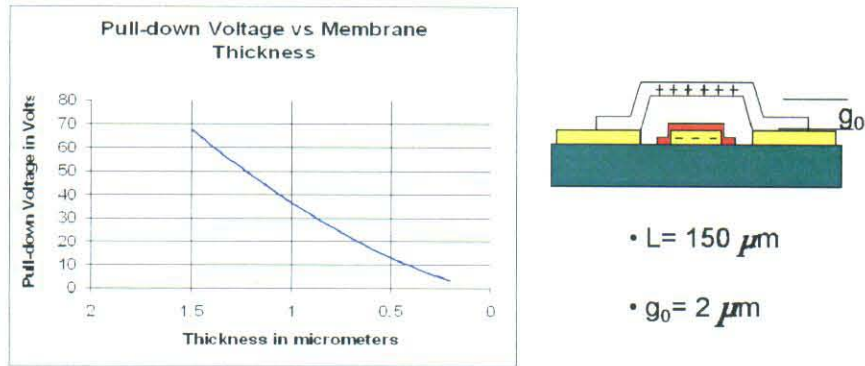
Figure 10: Measured pull down voltage V_p as a function of the actuators membrane thickness

Since the HTS switch operates around 77 K, the pull-down voltage (V_P) was measured as a function of temperature to determine how much K_s would be affected by operating at 77K. Both the pull-down and release voltages were measured as a function of temperature for the actuator given. The results of the measurements are shown in Figure 11. The results show that V_p increases as temperature decreases. The increase in V_P with decreasing temperature is related to material properties of the membrane and indicates that Young's modulus is changing as a function of temperature causing an increase in K_s.
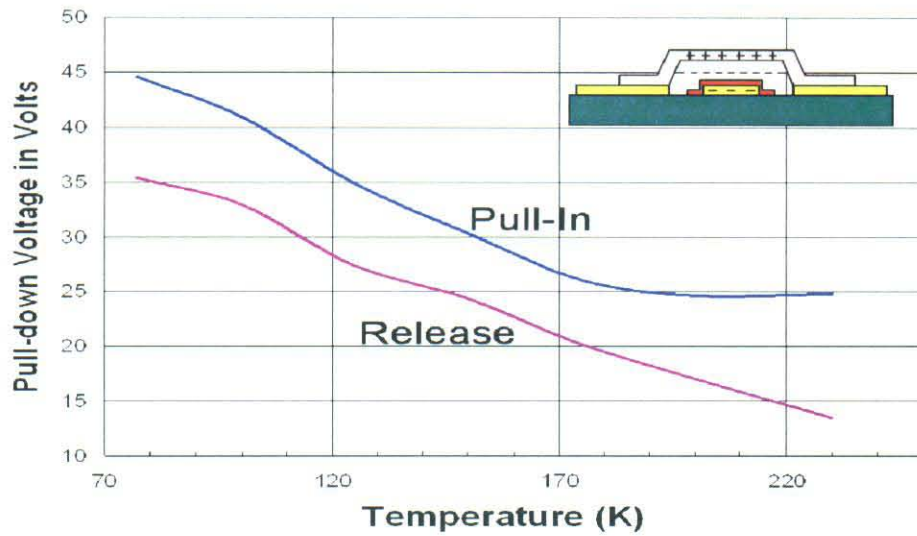
Figure 11: Pull down and release voltages versus temperature

An example of the HTS-MEM switches that were fabricated is shown in Figure 12. The fabrication process is compatible with standard MEM foundry technology.

11
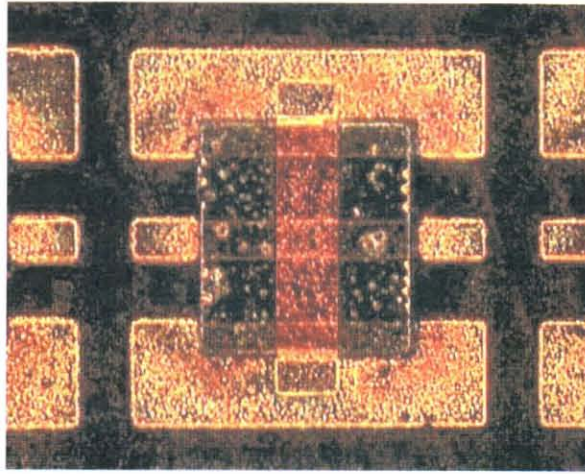
Figure 12: Photograph of HTS-MEM Switch

The microwave properties of the switches were characterized at 77K and those results are given in figure 13(a). Figure 13 (a) shows the measured and simulated results for the insertion loss of the switch for the membrane in the up position and the switch membrane in the down position. The simulated insertion loss is predicted to be greater than 12 dB for the switch in the down state and less than 1 dB for the switch in the up state between 10 and 20 GHz. The measured results show the insertion loss for the switch is between 7 and 13 dB in the down state and less than 2 dB in the up state between 10 and 20 GHz. Since the measured response for the switch in the up state was similar to simulation and there was a large difference between the measurement and simulation for the switch in the down state, the insertion loss for the switch was simulated again changing the capacitance value for gap between the membrane and the CPW transmission line in the down state. The results of the simulation are shown in figure 13(b). The results show a gap capacitance between 0.5 and 1.0 pF is needed for the measured results to agree with the simulation for the actuated state.
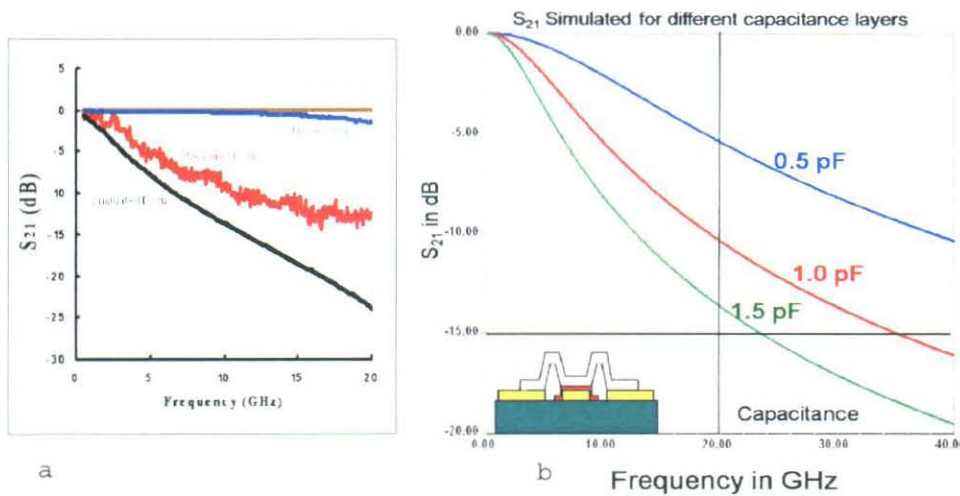
Figure 13:(a) Comparison of measured and simulated insertion loss (S21) response for the up and down states of HTS-MEM switch. (b) Simulated insertion loss response for the down state of the HTS-MEM switch using for a range of capacitance values for the gap between the membrane and the CPW transmission line.

12

2.0 LEFT-HANDED ELECTRODYNAMICS AND MICROWAVE MESOSTRUCTURES

2.1 Introduction

In 1968 V. G. Veselago[13] proposed that if materials exist with simultaneous negative electric permittivity (ε <0) and negative magnetic permeability (μ <0), they would have unique properties, including negative refractive index. Veselago described such a medium as a "left-handed material" since the electromagnetic properties of the medium form a left-handed system. It was approximately 30 years later when Veselago's premise of propagation thru a medium with $\varepsilon < 0$ and $\mu < 0$ was put to the test. Natural materials exist that either have a $\varepsilon < 0$ or $\mu < 0$, but no materials exist with $\varepsilon < 0$ and $\mu < 0$ at the same frequency in the electromagnetic spectrum. Materials such as ferrites exhibit a $\mu < 0$, but require a magnetic bias field to control the frequency at which $\mu < 0$. In nature a plasma exhibits $\varepsilon < 0$, and metals can be modeled as a plasma based on the Drude[14] model. John Pendry developed an effective medium model[15] allowing a wire grid to be treated as a plasma. Figure 14 shows his wire grid and the equations used to define the grids effective parameters, charge density, mass, and permittivity. The model defined an effective charge density n_{eff} for the wire grid based on the charge density (n) of the wire, the period (a) of the grid and the radius r of the wire. The effective mass m_{eff} of the charge density is also related to the radius r and the period (a) of the wire grid. Using the n_{eff} and m_{eff} the relationship of an effective permittivity is defined ε_{eff} is and the plasma frequency ω_p is predicted.

.ia Model

$$m_{eff} = \frac{\mu_0 \pi r^2 e^2 n}{2\pi} \ln\left(\frac{a}{r}\right)$$

$$\varepsilon_{eff} = 1 - \frac{\omega_p^2}{\omega(\omega + i\gamma)}$$
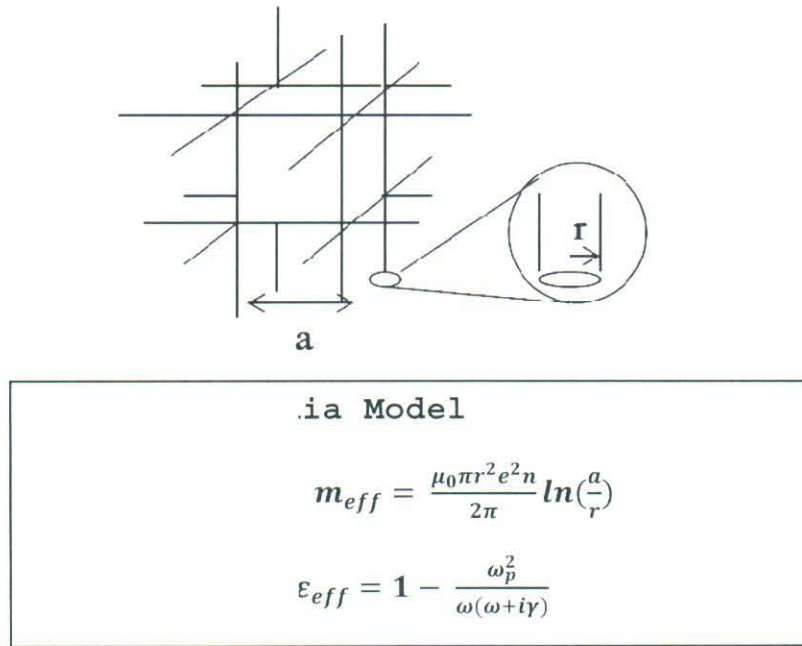
Figure 14: Pendry's wire grid and effective media model[15]

Pendry also developed a model that could predict a resonant frequency, at which a split-ring-resonator[16] (SRR), would have a $\mu < 0$. In Figure 15 the real and imaginary parts of the permeability μ for the SRRs magnetic resonance is shown. In the figure $\mu < 0$ when $\omega = \omega_0$ and $\mu = 0$ for $\omega > \omega_0$ where ω_0 is resonant frequency of the SRR.

Gyrotropic Media
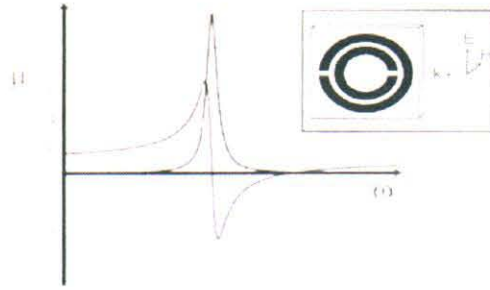
Figure 15: Pendry's plot for the real and imaginary part of μ the split-ring-resonator showing where Re(μ) < 0

$$\mu_{eff}(\omega) = 1 - \frac{F}{1 + \frac{2\sigma i}{\omega r \mu_0} - \frac{3}{\pi^2 \mu_0 \omega^2 C r^3}} \qquad \text{eq(2.1.1)}$$

Equation (2.1.1) is Pendry's equation for the effective permeability $\mu_{eff}(\omega)$ as a function of frequency where F is a fractional volume of the unit cell occupied by SRR[16].

In May of 2000 D. R. Smith et al.[17] demonstrated the first such "left-handed" (ε <0, μ <0) metamaterial. The left-handed metamaterial was comprised of discrete SRR and wire-posts. The SRR-wire-post medium is commonly referred to in the literature as left-handed (LHM), negative index (NIM), or double negative (DNG) metamaterial. Other structures have been designed with ε <0 and μ <0. An element shaped like Ω for instance provides both ε <0 and μ <0 in a single element[18]. There has been theoretical and computational work analyzing SRR and other resonant structures at microwave frequencies[19-21] and considerable additional effort to extend the NIM concept into the optical region of the electromagnetic spectrum.[22-24]

2.2 Negative Refractive Index

Our objective was to determine if the negative refraction of the SRRs and wire posts demonstrated by R. A. Shelby et al[25] met Veselago's criteria for an actual "left-handed material". We initiated a study to verify the required properties of the negative index metamaterial (NIM), which has to have a phase velocity anti-parallel to its group velocity, be highly dispersive, both ε and μ have to be simultaneously less than zero, and to understand the NIMs loss mechanism. The anti-parallel phase and group velocity causes electromagnetic radiation to refract to the same side of the normal as the incident electromagnetic radiation. This is one of the conditions for a negative refractive index, but not the only way electromagnetic radiation to refract negatively. The radiation can be negatively refracted by diffraction. The unit cell dimension of the NIM structures demonstrated in this report were below the diffraction limit, ε and μ were simultaneously less than zero, and the electromagnetic radiation refracted to the same side of the normal as the incident radiation. Veselago's criteria for a "left-handed" medium were met, but were the NIM media really an effective medium that could be described by ε and μ? The experiments demonstrating negative refraction were performed in a scattering chamber, a parallel plate waveguide, where only the transmission response of the medium could be measured. To further understand the electromagnetic properties of NIM we fabricated a series of various elements providing μ < 0 in conjunction with wire-posts for providing ε < 0.

14

2.3 Elements and Fabrication

The SRRs, Greek keys, and wire-posts were fabricated on copper clad dielectric printed circuit boards (PCboards). PCboards having 3 different dielectric constants (ε) were used FR-4, FR-35 and PCboards made from a Teflon^{TM} based material. The thicknesses of the PCboards were either 0.75 mm or 0.25 mm. The FR-4 and FR-35 have a dielectric constant of 4.0 and 3.5 respectively with a loss tangent of 0.005. The Teflon based PCboards were produced by 3 different manufactures Rogers Crop., Taconic, and Arlon. All the teflon based PCboards had a dielectric constant of 2.2 and a loss tangent of 0.002. A picture of a typical PCboard with SRRs and wire-posts is shown in Figure16. The SRRs are printed on the one side of the PCboard and the wire posts are printed on the other side of the PCboards.
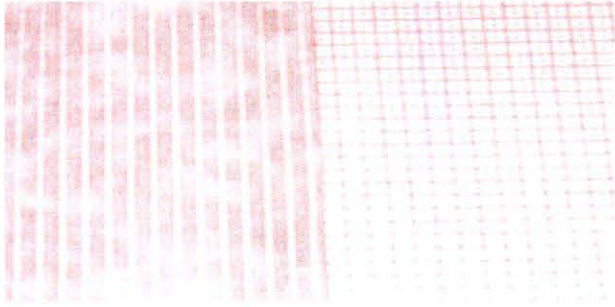
Figure 16: Shows both sides of an etched pcboard where nested SRRs etched into the copper on one side of the pcboard and the wire posts etched into the other side of the pcboard.

Figure17 shows the different styles of metallic inclusions SRRs, Greek key, and metal posts used to measure the electromagnetic properties of the media. These inclusions were used to experimentally study and better understand the fundamental electromagnetic behavior of these composite mesoscopic media.
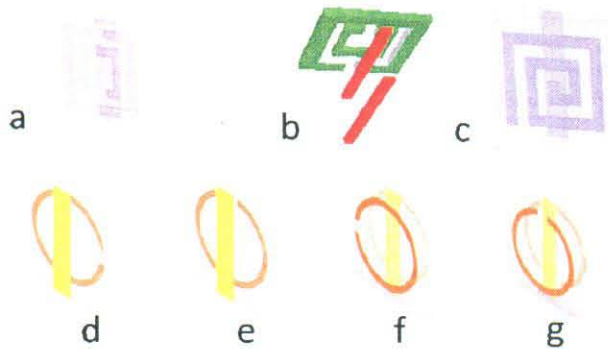
Figure 17: (a) is the standard SRR and wire-post element similar to R. A. Shelby et al.[25] , (b) is the element designed by Boeing and used in the DARPA Metamaterials Program, (c) is the Greek-key wire-post element, (d and e) are a single circular SRRs, (f and g) are balanced-SRR wire-post elements.

Figure 17 (a) shows the standard nested-SRR and wire-post element where one SRR is placed inside the other SRR. The nested-SRR wire-post element was commonly used to study the electromagnetic behavior of NIM media. Figure 17 (b) is the element designed by Boeing and used in the DARPA Metamaterials program to be measured by the Mayo Foundation, the Navy and the Air Force to validate negative refraction in the SRR-wire-post medium. In Figure 17 (c) is the Greek-key wire-post element, we used to validate Snell's law[26]. Figure 17 (d and e) are a single circular SRR-wire-post elements and Figure 17 (f and g) are the balanced-SRR wire-post elements used to study the bi-anisotropic and anisotropic behavior NIM media discussed in section

15

2.4.4. The balanced-SRR wire-post elements are rings of the same size parallel to each other with their gaps opposite each other along the circumference.

SRR dimensions	O.D. mm	I. D. mm	line width mm	gap mm	post mm	Cell = a , b , c mm		
circle								
Single-SRR	1.7	1.45	0.25	0.58	0.76	4.1	4.1	3.4
Balanced-SRRs	1.7	1.45	0.25	0.58	0.76	4.1	4.1	3.7
square nested -SRR	Outer length mm	Inner length mm						
	2.69	2.18	0.25	0.305	0.76	3.7	3.7	3.4
					Posts/ea.			
Boeing square SRR	2.2	1.1	0.2	0.3	0.3	2.68	2.68	2.68
swiss roll	Line length	spacing mm		# of turns				
	2.03	0.25	0.25	2	0.5	3.2	3.2	3.2

Table 1: The dimensions for the SRRs, Greek-key, wire-posts, and the dimensions.

The dimensions of the different NIM elements, such as SRRs and Greek Keys, and their unit cells used to make the different media used in this study are in Table I. The types of structures fabricated from these elements are shown in Figure 18. Three basic media shapes were used: i) an egg crate, ii) a rectangular block (referred to as a slab), and iii) a wedge shaped prism.

Figure 18: egg crate, slab, and wedge-prism structures fabricated.

2.4 Negative Refractive Index Media Measurements

2.4.1 NRI Waveguide Measurements

Our study of left-handed or negative refractive index metamaterials started in 2002. The study focused on the fundamental electromagnetic properties of NIM mesostructures in order to establish a basic understanding of their electromagnetic properties. We fabricated SRR-wire-post egg crate structures to be used in waveguide measurements. The egg crates were fabricated with of Taconic RF-35, FR-4, and Rogers 5880 duroid discussed in the previous section (element fabrication). At

that time little was understood about the SRR-wire-post medium except, its permeability and permittivity could be simultaneously less than zero according to the literature[15,16,17]. Our initial measurements performed on the egg crate structures were done using X-band waveguide operating between 8 and 12 GHz. A block diagram of the measurement setup is shown in Figure 19(a).
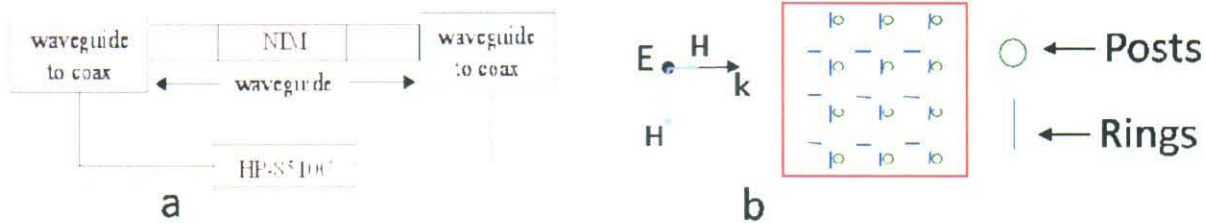
Figure 19: (a) shows measurement waveguide setup and (b) shows a diagram of the egg crate in the waveguide and the propagating TE-wave where the transverse E-field is out the page and the longitudinal and transverse components H-field vector is shown. The SRRs are represented by the blue lines and the wire posts by green circles.

The egg crate medium was designed with $\varepsilon < 0$ and $\mu < 0$ to occur above the 6.5 GHz cutoff of the waveguide. The egg crate medium was also designed with SRRs in 2 planes one parallel to the direction of propagation and the other perpendicular to the direction of propagation. To excite the SRRs resonance in the egg crate medium the magnetic field of the propagating wave threaded the SRRs. Figure 19(b) shows a diagram for the egg crate, waveguide, and the propagating wave in the waveguide. The propagating wave is a transverse electric (TE) wave, which means the electric field is perpendicular to the direction of propagation, but the magnetic field both has a longitudinal and transverse component. The diagram in Figure 19(b) it shows that the electric field is coming out of the a page perpendicular to the direction of propagation and parallel to the wire-post such that the wire posts create a medium with $\varepsilon < 0$. The diagram also shows the transverse and longitudinal components of the magnetic field in the plane of the page. The transverse and longitudinal components of the magnetic will thread the SRRs to excite the resonance producing $\mu < 0$.

The X-band waveguide is a closed measurement system, which allowed return and insertion loss of the medium to be measured. The reflection and transmission measurements for an egg crate medium are shown in Figure 20(a). Since measurement setup is calibrated, the reflection measurement is the return loss from the medium and the transmission measurement is the insertion loss in the medium. The result in Figure 20(a) shows resonances at 10GHz and 11GHz for the SRRs and wire-posts. The resonance at 10GHz is not as pronounced as the resonance at 11GHz. At 10GHz the return loss and insertion loss are approximately 7 dB and 35 dB respectively. For the 11GHz resonance average return loss is about 8 dB and an average insertion loss is about 15 dB. The 7 and 8 dB return loss for the 10 and 11 GHz resonances respectively show an impedance mismatch for the egg crate medium indicating the amount of incident power reflected. The insertion loss for the 10GHz resonance is also higher than that at 11GHz by 20 dB for the 10 GHz resonance. The measurements yield approximately 44% of absorption of power for egg crate at 11GHz.
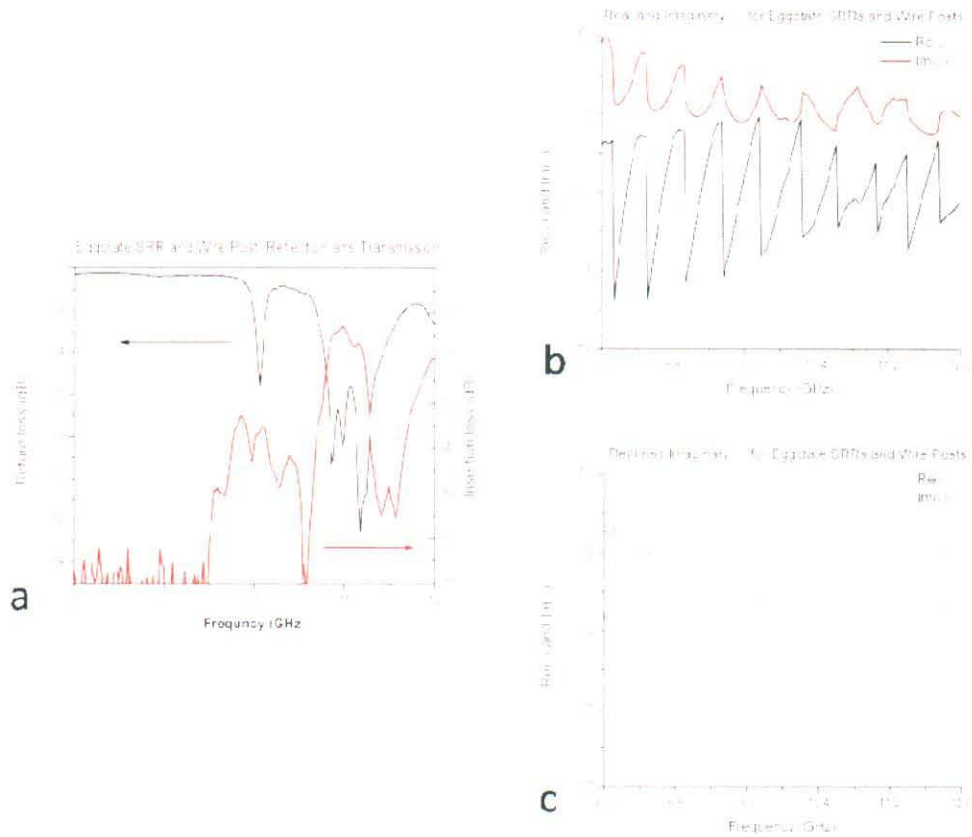
Figure 20: (a) shows the return loss (reflected power) and the insertion loss (the transmitted power) for SRR-wire-post egg crate medium. (b) shows the real and imaginary part of μ and (c) shows the real and imaginary part of ε for the medium.

At microwave frequencies a Nicholson and Ross[27] extraction is used to calculate ε and μ from the measured scattering parameters. The Nicholson and Ross extraction assumes that the material or medium being measured is homogenous and continuous. The SRR-wire-post egg crate medium meets the criteria for being continuous with a periodicity less than $\lambda/10$, but treating the egg crate as a homogeneous medium is a concern. The Nicholson and Ross extraction returned negative values for the imaginary part of ε. The imaginary parts of ε and μ account for the losses in the medium. The result of the extraction for the egg crate medium is shown in Figure 20 b and c. In the figure the values ε and μ oscillate at about 400MHz and are 90° out of phase with each other. The extraction has an ambiguity where it cannot tell the difference between a propagation length of one wavelength or integer multiples of wavelength. Thus, high dielectric materials or long sample lengths like the egg crate make it more difficult to accurately extract their constitutive parameters from the media. Other measurements are necessary to determine the validity of the results of the extraction.

2.4.2 Free Space Negative Refraction Measurements

As part of the DARPA's Metamaterials program a wedge shaped prisms were fabricated using the SRR-wire-post elements in Figure 17 (b) by Boeing. DARPA wanted verification that the SRR-wire-post element Boeing was using in its media actually exhibited negative refraction similar to Shelby et al[25] demonstration of negative refraction. The SRR-wire-post wedge shape prisms were circulated between the MAYO Research Foundation, the Air Force Research Laboratory, and the Navy to demonstrate the negative refraction. Along with the SRR-wire-post wedges were identical

Teflon™ wedges shown in Figure 21. Since the grade of hypotenuse increased in unit cell steps of the SRR-wire-post due their mesoscopic nature, the Teflon wedges were fabricated with steps along their hypotenuse to match the SRR-wire-post wedges.
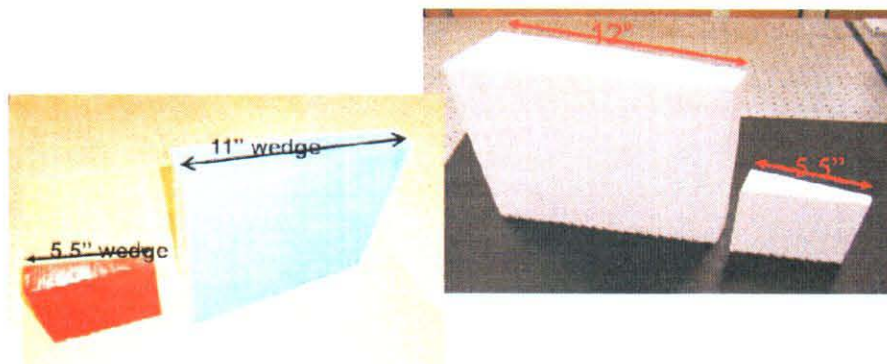
Figure 21:NRI and Teflon wedge-prisms fabricated by Boeing for the DARPA Metamaterial program.

Since the Boeing wedges were so large, it required the measurements to be made in free space rather than a waveguide. To make the free space measurements, we used the anechoic chamber at our Ipswich site. Figure 22 is a picture of the anechoic chamber. The free space measurement setup produced an incident TEM wave. The measurement setup in the anechoic chamber allowed frequency response of the wedge to be measured from 6 to 18 GHz. A baffle was built to center the wedge in the transmitted beam and block the part of beam that exceeded the aperture of the wedge. The baffle and wedge are also shown in Figure 22.
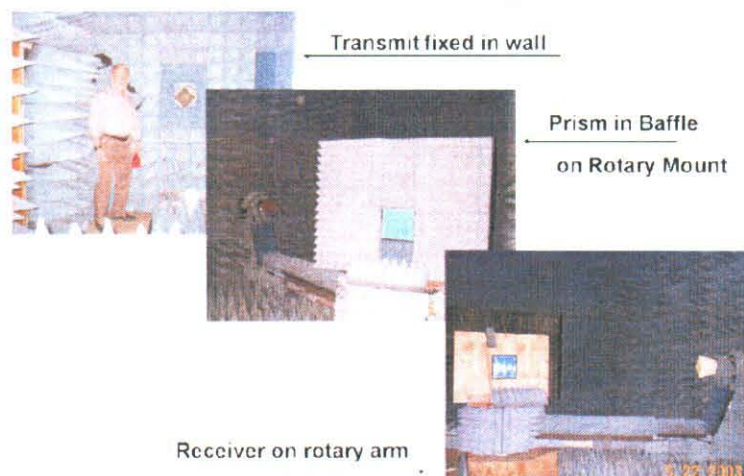
Figure 22:Shows the anechoic chamber with the transmit antenna mounted in the wall of the chamber, the mount with the baffle which is also capable of rotating, and the rotary arm where the receive horn is mounted.

A block diagram of the measurement setup for the anechoic chamber is shown in Figure 23(a). The diagram shows the relative position of the transmit and receive antennas and the baffle with a wedge as setup in the chamber. The diagram also shows the HP-8530 transceiver used to transmit and receive the microwave signal. The receive antenna is mounted on a rotating arm, which allows the pattern of the beam to be measured as a function of angle as well as the frequency response of the wedge.

19

a   b
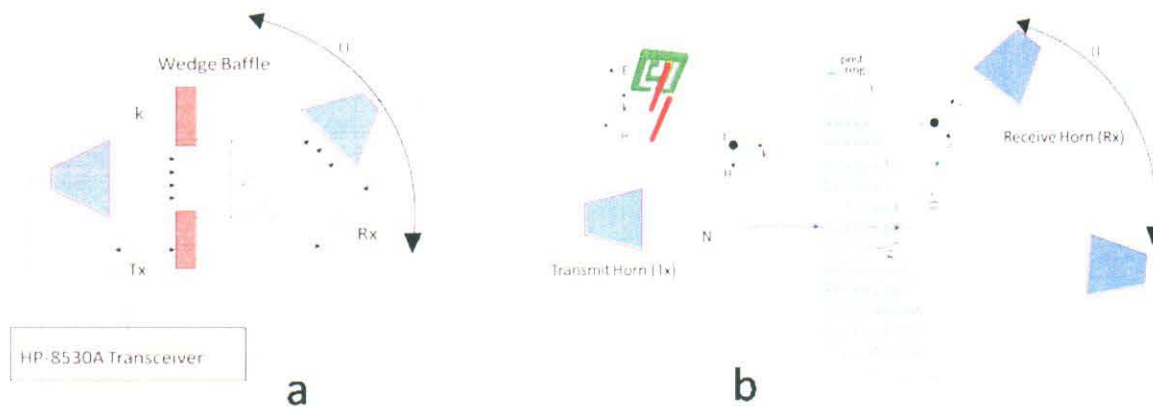
Figure 23: (a) Shows a block diagram of the free space measurement setup used in the anechoic chamber. The diagram shows the typical position of the transmit antenna (Tx) relative to the baffle, wedge, and receive antenna (Rx). The diagram also indicates how the HP-8530 transceiver is connected to the antennas. (b) shows the cross section of a wedge indicating planes of SRRs and wire-posts and the TEM conditions for negative refraction to occur. The insert of the Boeing cell shows the TEM at the cell level.

Figure 23 (b) shows a diagram of a cross section of wedge, transmit and receive antennas, and the polarization of the transmitted beam. The cross section of the wedge in the diagram depicts the PCboard as solid lines that extend from the base of the wedge to its hypotenuse. With wire-posts are positioned along one side of the PCboard and the SRRs on the other side, where the wire-posts are shown as a circular cross section of a cylindrical wire and the SRRs are shown small line segments on the other side of the PCboard across from each of the wire-posts. The vector diagram for the TEM wave shows the electric field (E-field) coming out of the page and parallel to the wire-posts and the magnetic field (H-field) normal to the plane of the SRRs allowing the H-field to thread the rings. The k vector represents the direction of propagation for the TEM wave. Negative refraction is defined by the incident and the refracted angle of the propagating wave relative to the normal at hypotenuse. If the incident wave at the hypotenuse refracts to the same side of the normal as the incident wave as shown in the ray diagram in Figure 23(b) it is defined as negative refraction. When the incident beam at the hypotenuse of the wedge is refracted to the opposite side of the normal it is defined as being positive refraction.

The results of the measurements SRR-wire-post wedge and Teflon wedge are shown in Figure 24 (a and b). The results are plotted as a function of angle, at 14.1 GHz, relative to the normal of the hypotenuse ($0°$) where negative angles are to the left of the normal as in Figure 23(b) indicating negative refraction and positive angles are to the right of the normal indicating positive refraction. Figure 24(a) shows the peak of the beam is at approximately -15° for the SRR-wire-post wedge indicating negative refraction. Figure 24(b) shows the peak of the beam is at approximately18° for the Teflon wedge indicating positive refraction.
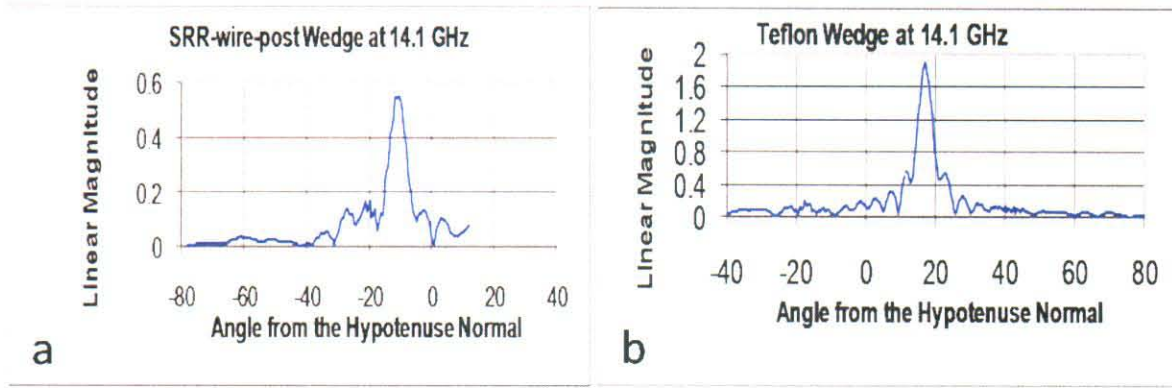
Figure 24:Provides the beam pattern angular measurements made at 14.1 GHz; (a) for the Boeing SRR-wire-post wedge showing the peak of the beam pattern at -15° indicating negative refraction for the SRR-wire-post wedge, (b) for the Teflon wedge where the peak of the beam pattern is at 18° indicating positive refraction.

Since the SRRs and wire-posts are only in one plane of the wedge, we rotated the polarization of the TEM wave by 90° so the E-field was normal and the H-field was parallel to the wire-posts Figure 25 (a) is a diagram showing the measurement configurations used to characterize properties of the wedge other than its negative refraction. The diagram shows the 2 cases for the linearly polarized wave illuminating the wedge. The first case is with the E-field parallel to the posts in the wedge, which produces the negative refraction behavior in the wedge. The second case is with the E-field perpendicular to the posts in the wedge. In the second case the conditions for generating $\varepsilon <$ 0 and $\mu < 0$ are not met thus producing positive refraction. The beam pattern for SRR-wire-post wedge was measured again at 14.1 GHz with the E-field perpendicular to the posts.
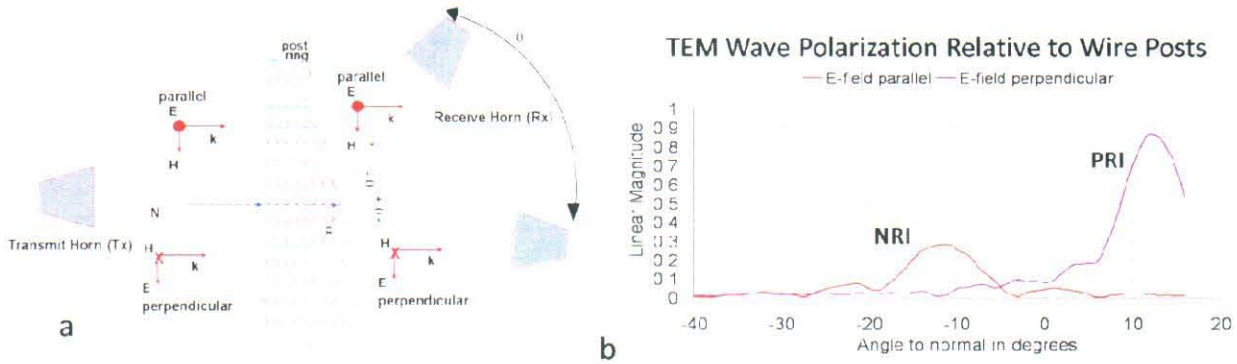
Figure 25: (a) Diagram for E-field orientation relative to the post in the wedge. (b) The TEM wave vector marked parallel has its E-field parallel to the posts refracts to the -Θ side of the normal (negative refraction) and the TEM wave vector marked perpendicular has its E-field perpendicular to the posts and refracts to +Θ side of normal (positive refraction)

The measurement results for both cases are shown in Figure 25 (b). The results show that the beam refracts positively as expected and no peak in the beam pattern is observed at the angle where the negative refraction occurs in the wedge[28] for the parallel polarization. Since no peak in the beam pattern was observed in at negative angles for the positive refraction case, diffraction or scattering from the SRRs and wire-posts is not a likely explanation for the negative refraction observed in the SRR-wire-post medium. This shows the importance of polarization on the excitation of the negative refraction behavior of the wedge. Since the free space measurements allowed us to control the orientation of the polarization of both Tx and Rx antennas, we measured

21

the co- and cross- polarization for the medium. The diagram for the co- and cross-polarization measurement is shown in Figure 26. The co-polarization is measured for the wedge when the plane of E-plane of the transmit and receive antennas are vertical and parallel to the wire-posts as shown in the diagram. In the cross-polarization measurement the E-plane of the transmit antenna remains vertical (parallel to the posts) and the E-plane of the receive antenna is rotated 90° or horizontally (perpendicular to the posts) as shown in the diagram. This places the E-plane of receive antenna perpendicular to the E-plane of the transmit antenna forming crossed planes.
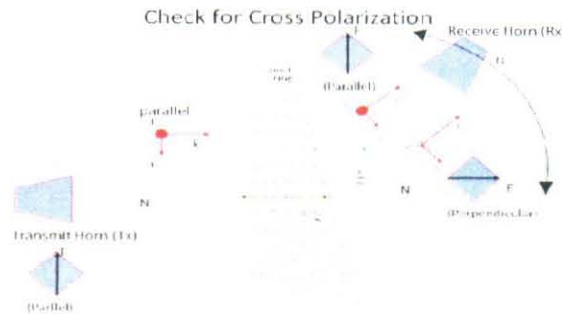
Figure 26: Is a diagram of how the Tx and Rx antennas are oriented for the co- and cross-polarization measurements. The co-polarization orientation is when the Tx and Rx antennas E-field parallel to each other like aligned polarizers and the cross-polarization orientation is when the E-field of the Rx antenna is perpendicular to the E-field of the Tx antenna in a crossed field orientation like crossed polarizers.

The results of the co- and cross-polarization measurements are shown in Figure 27 (a and b). Figure 27 (a) shows the co-polarization measurement and Figure 27 (b) shows the cross-polarization measurement. The results show almost a 7:1 ratio in the peak amplitudes of the beams for co- and cross- polarization.
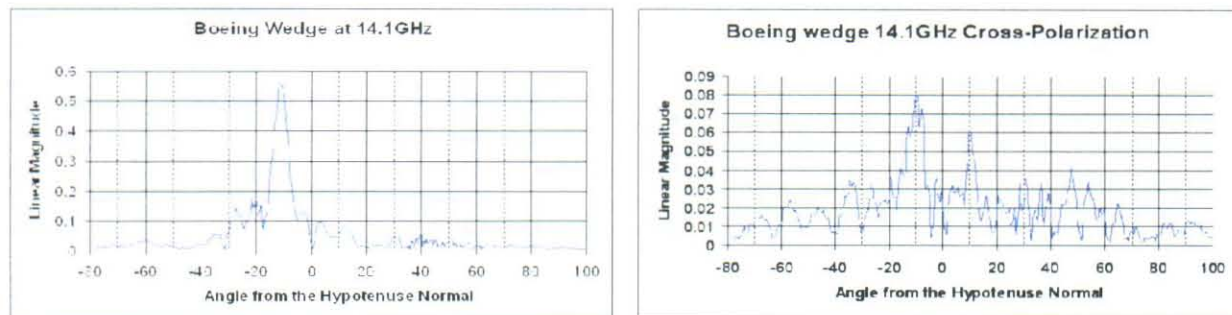
Figure 27:(a) shows the co-polarization measurement of the wedge (the negative refractive response of the wedge) and (b) shows the cross-polarization measurement providing an 86 % extinction of the beams peak signal for the crossed polarized E-fields.

These measurements indicate that the wedge has radiative losses as well as ohmic losses for the negative refractive behavior of the wedge. These results show the importance of making free space measurements on metamaterials structures, and studying the polarization behavior and radiative loss mechanisms that metamaterials exhibit. The polarization properties of metamaterials will be discussed further in section 2.4.4.

2.4.3 SNELL' S LAW Metamaterial Measurements

According to Veselago's paper a left-handed or negative refractive index metamaterials would obey Snell's law. Though a number of measurements were made demonstrating negative

refraction, the measurements were made for a single angle of incidence. These measurements have been accepted as proof of Snell's law by some and others have argued that the negative refraction observed in NIM media is due to diffraction or guided wave phenomena in the media. We thought about the different arguments for negative refraction, starting with the diffraction. The SRR-wire-post elements and the periodicity of their unit cell are well below the geometrical diffraction limit. The period steps in hypotenuse of the wedge would also not produce a diffraction pattern that could account for the observed negative refraction. Guided wave structures like delay line lenses are based on the phased delay produced by the waveguide elements that make up a structure like a delay line lens. Both diffraction and guided wave media do not obey Snell's law. We proposed an experiment using the free space measurement setup Figure 22 and 23 (a) that would allow us to change the angle of incidence at the transmitted microwave beam at the entrance face of the wedge and measure the exit angle form the hypotenuse of the wedge. If observed negative refraction was a diffraction pattern or a guided wave pattern the measured exit angle from the wedges hypotenuse would not follow Snell's law. Only a brief summary will be discussed here. The experimental results validating Snell's law were published by Derov etal[26].

Three Greek key NIM prisms with different apex angles were constructed to investigate the consistency of the metamaterial construction technique and the refractive index of the metamaterial. The Greek-Key element and unit cell dimensions can be found in Table I. Since the negative index is highly frequency dependent, the frequency at which the refractive index (n) equals -1 is a useful standard for comparison. The frequency, at which n = -1, is when the negative refraction angle is equal to the apex angle of the wedge. For all three Greek-key wedges, the difference in the frequency, at which n = -1, occurs is between 10.1 and 10.2 GHz. The agreement is within 1% in frequency shows consistency of the prism fabrication and of the on-axis index.

Measurements were made with oblique entrance angles at selected frequencies. The electric field remained parallel to the posts, but the magnetic field did not remain perpendicular to the plane of the substrates as entrance angle changed. A diagram showing the normal entrance angle and an oblique entrance angle are show in Figure 28(a). The results for a Greek-key wedge with an apex angle of 18° and a positive refractive index Teflon wedge with a 32° apex angle are plotted in Fig. 28(b) showing the exit angle, measured relative to the normal axis of the wedges hypotenuse, as a function of entrance angle, measured from the normal to the first face.
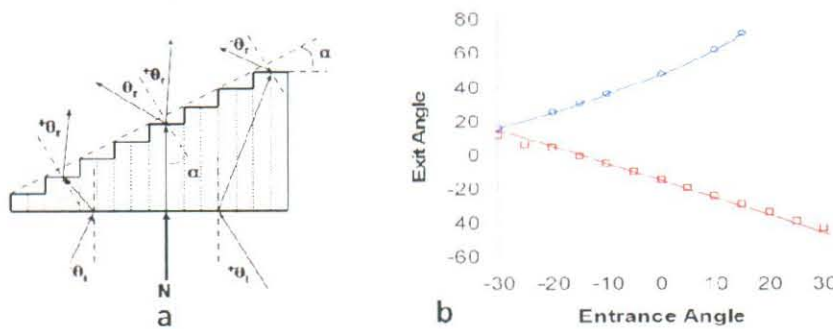
Figure 28: (a) wedge diagram showing the convention for determine for positive and negative refraction angles in air applied to Snell's law for determining the exit angle and (b) the red curve shows the Snell's law fit to the a Greek-key wedge with a 18° apex angle and the blue curve is a Snell's law fit to the Teflon wedge.

The solid lines shown in Fig. 28(b) for the Teflon and Greek-key wedge were calculated using Snell's law with the refractive index determined at the 0° entrance angle and calculating the exit angles based on the entrance angles. Snell's law is in good agreement with the measured exit angles for both the Teflon and Greek-key wedges.

2.4.4 The Polarization behavior of the SRR-wire-post Medium

To study the polarization behavior in NIM media, the nested-SRR-wire-post element (a) in fig. 17 used to design and fabricate the wedge and slab as shown in fig. 18. The transmission response of the wedge was measured as a function of frequency and angular dependence of the transmitted beam angle. The measurement results are shown in Figure 29. As seen in the figure a peak transmitted beam for the wedge is observed between 13GHz at -20° and 15GHz at less than 0° indicating where negative refraction occurs in the wedge. From the results it was determined n = -1 at 13.5 GHz for the wedge.
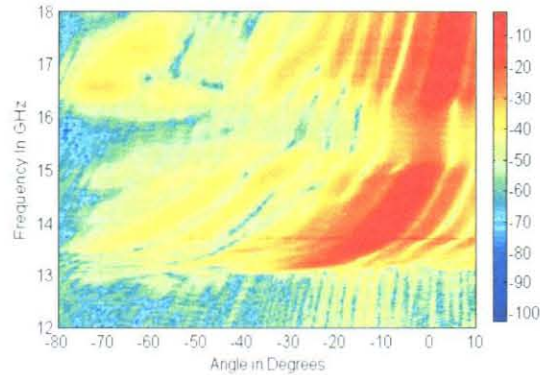
Figure 29: Transmission response of the nested-SRR-wire-post wedge as a function of frequency and angle.

The co- and cross- polarization measurements of the wedge were used as the starting point of the study using the same measurement setup as in Figure 26. This was used to measure the co- and cross- polarization of the wedge at 13.5 GHz where n = -1. The results of the measurement are shown in Figure 30.
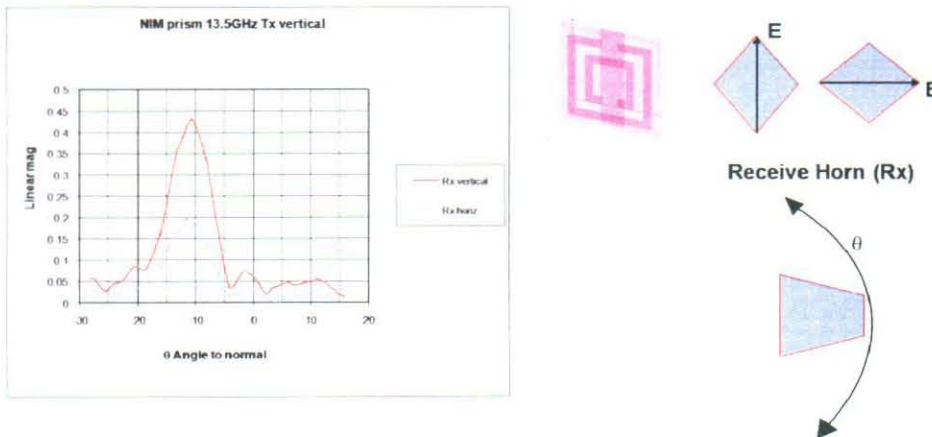
Figure 30: The red curve is the co-polarization and the blue curve is the cross-polarization of SRR-wire-post wedge at 13.5GHz and a diagram of the E-field for the receive horn is where the vertical and horizontal orientation of the E-field is the co- and cross-polarization respectively.

From Figure 30 it is seen that the amplitude of the cross-polarization is 40 % of the co-polarization amplitude. Since cross-polarization for the wedge was significant, the orientation of the beams polarization was mapped as a function of angle. To measure polarization as function of angle the Rx antenna shown in Figure 31 was rotated about its axis to change the angle of the E-fields orientation. The initial orientation for the Tx and Rx antennas was with their E-fields vertical to each other and parallel to the wire-posts in the wedge defining 0° for direction of polarization. During the polarization measurement the Rx antenna E-field was rotated through the

24

angle φ ±180° about the 0° reference as shown in Figure 31.
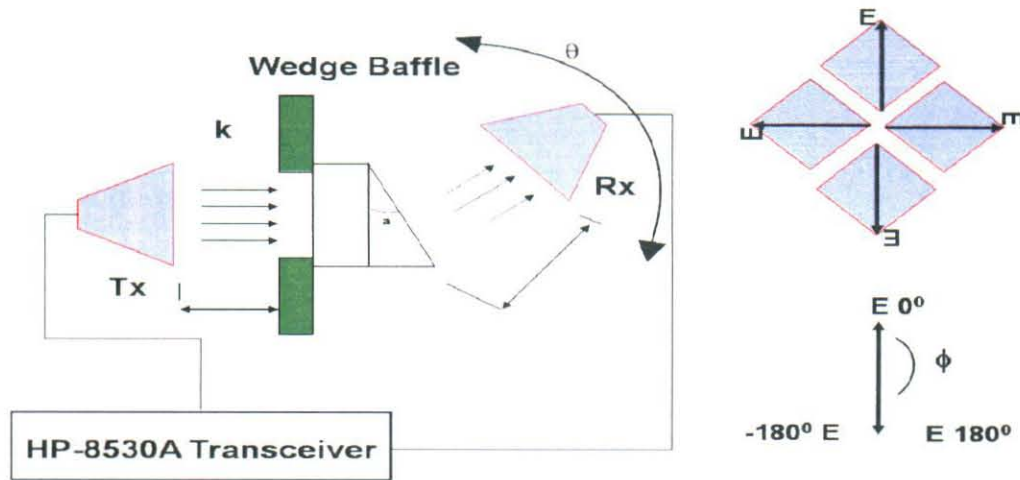
Figure 31: Setup used to map the E-field amplitude of the linearly polarized TEM wave after passing thru the NRI wedge medium. A diagram for the receive antenna defining 0° and ±180° for the angle φ.

The result of the polarization measurement is shown in Figure 32. The figure shows a plot of the transmitted power thru the wedge as a function of polarization angle. The data was fit using a |cosφ| function to determine the angle at which maximum power occurs. The plot shows maximum power occurs at 22° in the clockwise direction from the polarization angle of the Tx antenna. Indicating the nested-SRR-wire-post medium rotates of the linear polarized source beam as the beam passes thru the wedge.
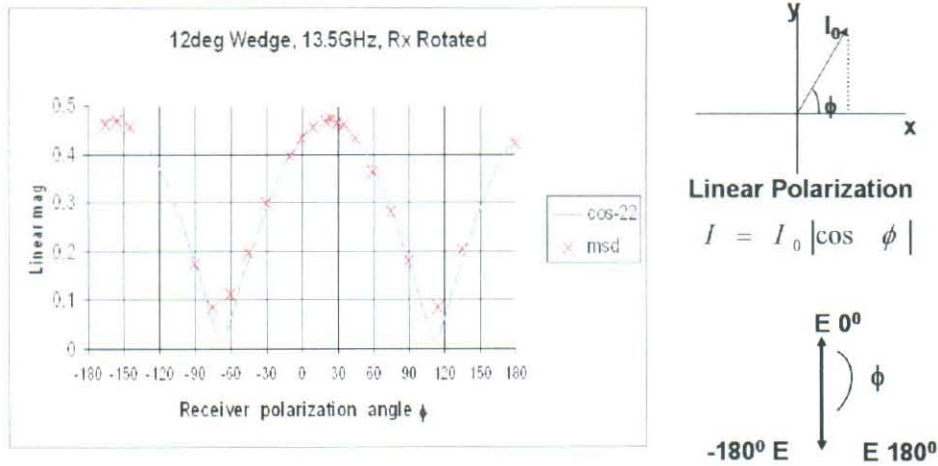
Figure 32: The amplitude of the E-field as a function of polarization angle φ fit to |cosφ|.

Since the E-field is rotated 22°, the question is, whether the wave changed from linearly polarized wave to an elliptically polarized wave. The results in Figure 32 place the major axis at 22° inferring the minor axis is at 112° for an ellipse. If the wave is elliptically polarized it should have right or left handed behavior. To determine if the wave had a right or left handed behavior a set of helical-antennas were designed and fabricated. One helical-antenna was designed to be right-

25

handed circularly polarized and the other antenna was designed to be left-handed circularly polarized. A picture of the helical antennas is shown in Figure 33. The helical antennas had a center frequency of their bandwidth at 13.8 GHz.

Figure 33: Left and right circularly polarized helical antennas, the right circularly polarized antenna has the pitch of the helix rotating in a clockwise direction and the left circularly antenna has the pitch of its helix rotating in a counterclockwise direction.

The helical antennas were characterized for their left- and right-handed extinction ratio and signal sensitivity. The measurements were made in the anechoic chamber in Fig. 22. The right- and left-handed extinction ratio was measured by selecting a left- or right-handed antenna for Rx and the opposite handed antenna for Tx. The measurements for a pair of left-handed antennas and for a right and left handed pair of antennas are shown in Figure 34 (a). Figure 34(a) shows the maximum amplitude of the power detected by the Rx antenna for the left-handed pair of antennas was 0.4 and the maximum amplitude of the power detected by Rx antenna for a left- and right-handed antenna pair was approximately 0.02, indicating a 20:1 extinction ratio for the left- and right-handed antennas. Using a linearly polarized transmit antenna the signal sensitivity of the helical antennas was measured to provide a baseline response for the antennas. The antennas sensitivity measurements are shown in Figure 34(b) a linearly polarized Tx antenna and a left- and right-handed Rx antennas. The measurements were performed at 13.8 GHz the frequency where the helical antennas had their best impedance match for 50Ω measurement systems. The results in Figure 34 (b) show a 14% difference in amplitudes between the left- and right-handed helical antennas for the power detected.

a

b
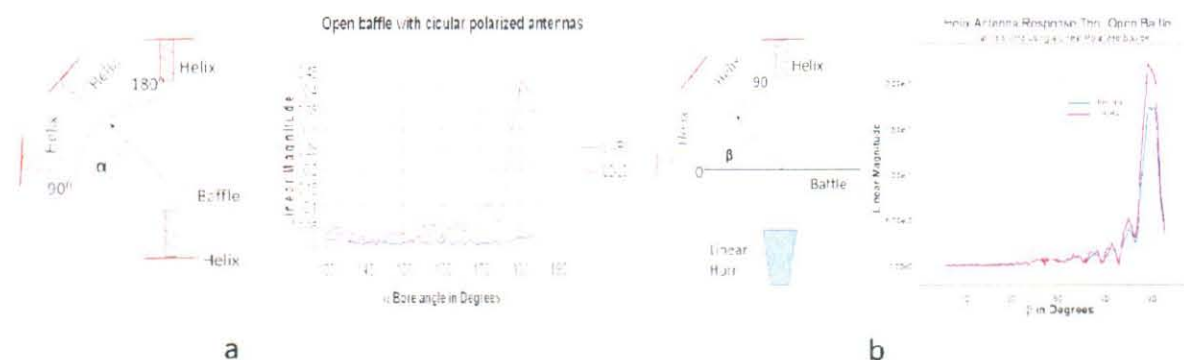
Figure 34: (a) Shows the beam pattern measurements for a set of left-handed helical antennas one for Tx and the other for Rx. The plot in (a) also shows the beam pattern measurement for a left-handed helical Tx antenna and right-handed Rx antenna used to determine their extinction 20:1 distinction ratio. (b) shows the beam patterns for a left- and right-handed helical antenna used as Rx antenna with a linearly polarized Tx antenna. The beam patterns show a 14% difference between the left- and right-handed magnitudes.

26

The NIM wedge was then characterized using the linearly polarized antenna as the Tx antenna with either the right-handed or left-handed helical antennas as the Rx antenna. Since the polarization rotation is related to the negative refraction of the wedge, the measurements were made at 13.5 GHz where n = -1 and the beam pattern were measured as function of angle. The results of the measurements for the linearly polarized source are shown in Figure 35(a). The results show the amplitude of the power measured by both the right-handed and left-handed helical-antennas is approximately the same. Indicating that the linearly polarized transmitted beam is neither right-handed or left-handed circularly polarized after passing through the wedge medium. Measurements were also made using i) a set of right-hand helical antennas for the Tx and Rx antennas and ii) a left-handed helical antenna for Tx and a right-handed helical antenna for Rx. The result of these measurements is shown in Figure 35 (b). Figure 35(b) shows the power measured by the helical antennas are similar whether a pair of right-handed helical antennas are used for the Tx and Rx antennas or a left-handed Tx antenna and a right-handed Rx antenna is used for the measurement. The results in Fig. 35(b) show that a circularly polarized beam passing thru this NIM medium will refract positively as well as negatively. This indicates that circularly polarized radiation passing thru the wedge loses its handedness.

a   b
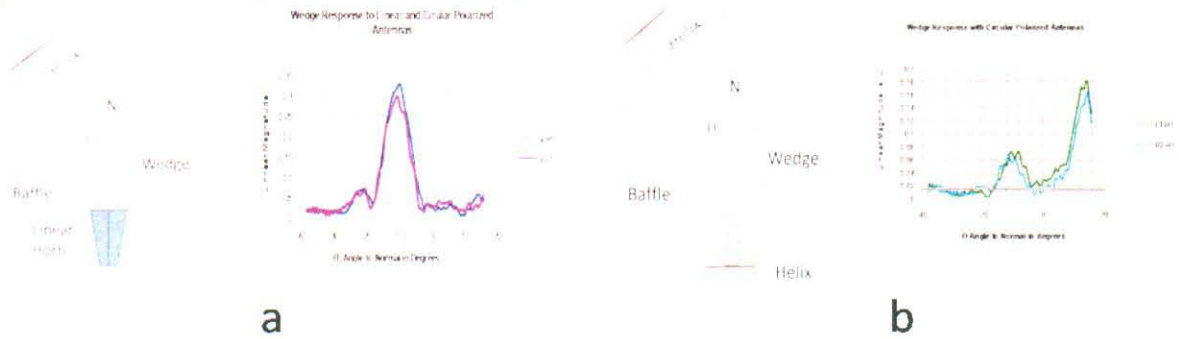
Figure 35: (a) Shows measured beam patterns for linear polarized Tx antenna and a left- and right-handed helical Rx antenna. (b) shows the beam patterns for i) a right-handed helical Tx and Rx antenna, ii) a right-handed helical Tx antenna and a left-handed Rx antenna and reference line for the maximum magnitude observed when a right-handed and a left-handed antenna measured in Figure 34 (a).

The positive and negative refraction shown in Figure 35 (b) is equivalent to rotating the E-field of the linearly polarized Tx and Rx antenna to a 45° angle relative to the posts in the wedge. In section 2.4.2 the cases for the orientation E-field parallel and perpendicular to the wire-post in the wedge were shown where either negative or positive refraction was observed depending on the orientation of the E-field. Since the polarization of the circularly polarized wave is rotating, the E-field of the wave will not be parallel or perpendicular to the wire-posts when the wave enters the wedge. This orientation of the E-field for the circularly polarized wave is similar to having the E-field of a linearly polarized wave enter the wedge at 45° angle. In Figure 36 (a) shows measurements for linearly polarized Tx and Rx with their E-field oriented 45° to the wire-posts and Figure 36 (b) shows the measurement helical antennas. Figure 36 (a and b) look similar, both figures show a negative and positive refraction in the beam pattern. These measurement results confirm that a wave exiting the wedge will be linearly polarized even if the transmitted signal into the wedge is circularly polarized.

a

b
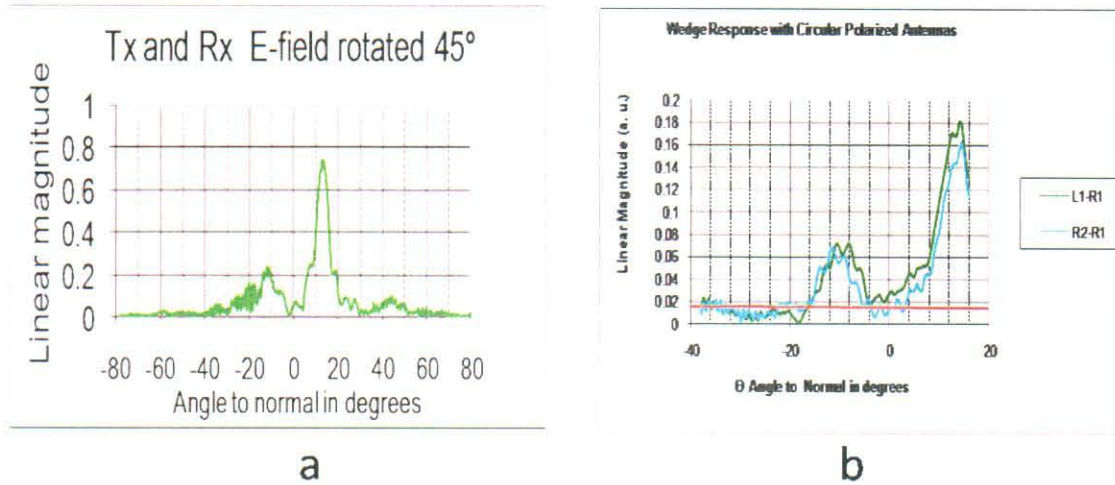
Figure 36: (a) Show the measurement for a SRR-wire-post with the Tx and Rx linearly polarized antennas at 45° and (b) is Figure 35 (b) for the readers convenience.

To account for the E-field rotation of a wave, observed in the co- and cross-polarization measurements, we measured the polarization behavior of the NIM slab with a thickness of 6 unit cells (22.2 mm) fabricated along with the wedge. We know the slab will exhibit negative refraction since it is made from the exact same material used in the wedge. Polarization measurements were made on the slab, but no rotation of the E-field of the wave was observed after passing thru the slab. To understand the result 3 more slabs were assembled with the thickness of 1, 3, and 16 unit cells (1unit cell = 3.7 mm). The 3 slabs were measured to see if the E-field of a linear polarized wave rotated after the passing thru the slabs. The results of the measurements are shown in Figure 37. The results show the polarization rotation is linear through the slab geometry. Though the 1-cell thick medium is a surface and not a bulk medium, its behavior is in agreement with measurements of the thicker slabs. The rotation of the E-field of the wave passing thru the wedge is similar to Faraday rotation in dielectrics.
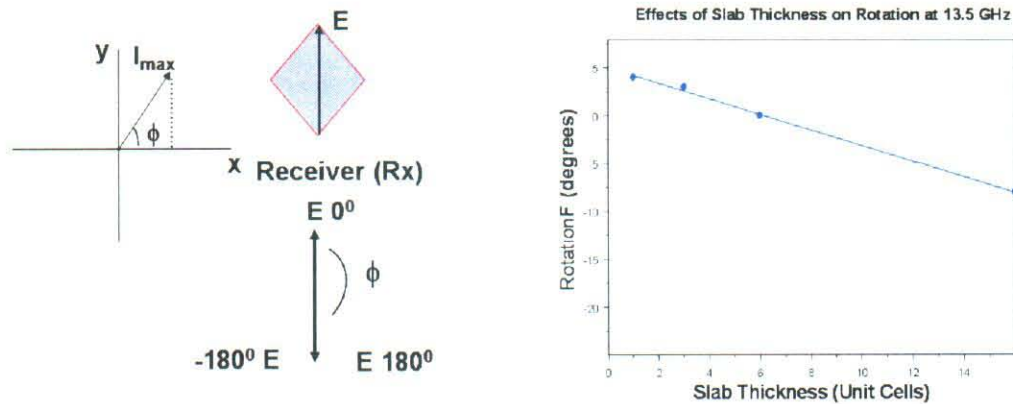
Figure 37: shows rotation of the E-field for a linearly polarized wave after passing thru a slab SRR-wire-post slab medium. The measured results show the E-field rotation is linearly dependent on the thickness of SRR-wire-post media.

2.4.5 The Bi-anisotropic behavior of SRRs

The bi-anisotropic properties of the SRRs in a NIM medium do relate to the polarization behavior

28

of served in our measurements. Bi-anisotropy means the electric and magnetic fields in Maxwell's equations are implicitly related through the constitutive parameters. For bi-anisotropy there are 4 tensors ε, μ, ξ, and ζ for the constitutive relationships, shown here

$$\bar{D} = \bar{\bar{\varepsilon}}\bar{E} + \bar{\bar{\xi}}\bar{H} \;\; and \;\; \bar{B} = -\bar{\bar{\zeta}}\bar{E} - \bar{\bar{\mu}}\bar{H}.$$

Maxwell's equations for bi-anisotropic media are given in equations 2.4.5.1 and 2.4.5.2.

$$\nabla \times \bar{H} = -j\omega\bar{\bar{\varepsilon}}\bar{E} - j\omega\bar{\bar{\xi}}\bar{H} \qquad\qquad eq.(2.4.5.1)$$

$$\nabla \times \bar{E} = j\omega\bar{\bar{\zeta}}\bar{E} + j\omega\bar{\bar{\mu}}\bar{H} \qquad\qquad eq.(2.4.5.2)$$

To show how bi-anisotropy affects the SRRs 3 single SRRs are shown in Figure 38 with a linearly polarized TEM wave propagating in different direction for each SRR. In Figure 38 (a) the wave is propagating into the plane of the page thru the ring. The E-field of the wave is in plane of the page and parallel to the gap of the ring. In this case the E-field induces a current in same direction in the two parallel sides of the ring without a gap. The currents cancel each other out and the ring does not resonate. The ring in Figure 38 (b) shows the direction of propagation for the wave is to the left in the plane of the page with H-field directed into the page threading the ring and the E-field of the wave is still parallel to the gap. In this case the H-field induces a circulating current in the ring exciting the resonance. The last ring Figure 38 (c) shows the wave propagating downward in the plane of the page. The E-field is in the plane of the page such that the E-field will cross the gap of ring and the H-field is into the page threading the ring. The E-field across the ring gap capacitively couples and the H-field inductively couples to the ring. Both fields produce a circulating current to drive the resonance of the ring. Since both the E-field and the H-field couple to the ring producing a resonance, the ring is considered bi-anisotropic. Any structure that couples both the E-field and H-field is considered to be bi-anisotropic.
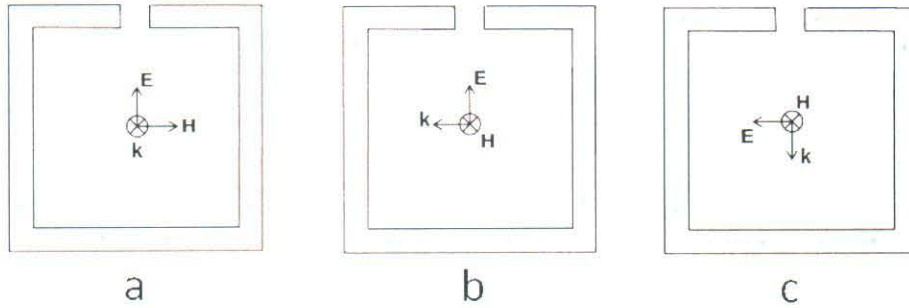
Figure 38: (a) shows currents induced be the insides of ring parallel the E-field, (b) shows the currents induced in the ring by the H-field, and (c) shows the currents induced by both the E- and H-field.

To relate the affect of bi-anisotropy to our measurements of the nested-SRR-wire-post medium, we applied the electric and magnetic dipole moments derived by Marquesé et al.[29] for the nested-SRRs. The set of electric and magnetic dipole moments derived by Marquesé et al. are shown in eqs (2.4.5.3).

$$p_x = \alpha_{xx}^{ee}E_x, \quad p_y = \alpha_{yy}^{ee}E_y + j\alpha_{yz}^{em}B_z \quad m_z = -j\alpha_{yz}^{em}E_y + \alpha_{zz}^{mm}B_z \qquad eqs.(2.4.5.3)$$

There are 2 electric dipole moments p_x and p_y and 1 magnetic dipole moment m_z and the E- and H-fields are implicit in p_y and m_z. We applied the dipole moments to the nested-SRRs in our wedge medium along with the orientation of TEM wave used in the measurements. The results are given in eqs. 2.4.5.4. All 3 dipole moments occur, but the E- or H-fields are explicit for each of the

dipole moments. The second electric dipole moment p_z is generated by a H-field.

$$p_x = \alpha_{xx}^{ee} E_x, \quad p_z = j\alpha_{zy}^{em} \mu H_y, \quad m_y = \alpha_{yy}^{mm} \mu H_y \qquad \text{eqs.}(2.4.5.4)$$

Since p_z only has a H-field term, it does indicate our nested-SRR-wire-post wedge medium is bi-anisotropic, but it is not clear how the properties of the wedge medium[30] relate to the bi-anisotropy of the SRRs.

Group theory has also been applied to metamaterial elements[31,32] such as SRRs. The theory is based on point group symmetry of the metamaterial elements. From the point group symmetry the tensor components for the constitutive parameters can be determined. The point group for the nested-SRR in our wedge is C_{2v}. Applying group theory to our nested-SRR-wire-post medium yields the following 4 tensor arrays describing its constitutive parameters and substituting the tensors into Maxwell's equations along with the orientation of TEM wave yields equations 2.4.5.1 and 2.4.5.2 for the wedge.

$$\bar{\bar{\varepsilon}} = \begin{bmatrix} \varepsilon_{xx} & 0 & 0 \\ 0 & \varepsilon_{yy} & 0 \\ 0 & 0 & \varepsilon_{zz} \end{bmatrix} \quad \bar{\bar{\mu}} = \begin{bmatrix} 1 & 0 & 0 \\ 0 & \mu_{yy} & 0 \\ 0 & 0 & 1 \end{bmatrix} \quad \bar{\bar{\zeta}} = \begin{bmatrix} 0 & 0 & 0 \\ 0 & 0 & \zeta_{yz} \\ 0 & 0 & 0 \end{bmatrix} \quad \bar{\bar{\xi}} = \begin{bmatrix} 0 & 0 & 0 \\ 0 & 0 & 0 \\ 0 & \xi_{zy} & 0 \end{bmatrix}$$

$$\nabla \times \vec{H} = -j\omega\varepsilon_{xx} E_x - j\omega\xi_{zy} H_y \qquad \text{eq.}(2.4.5.5)$$

$$\nabla \times \vec{E} = j\omega\mu_{yy} H_y \qquad \text{eq.}(2.4.5.6)$$

The coupling of the E and H fields is obvious in eq. 2.4.5.5 showing the bi-anisotropic behavior occurs in the wedge medium. The bi-anisotropic behavior indicated in eq.(2.4.5.5) and the electric dipole moment p_z in eq. 2.4.5.4 may account for the E-field rotation observed in section 2.4.4.

In Marquesé's paper he designed a set of anisotropic SRRs. The SRRs were made up of 2 rings the same size parallel to each other with the split in the rings oriented opposite each other along their circumference as shown in Figure 17 (f and g) referred to as balanced rings. To compare the difference between bi-anisotropic and anisotropic behavior, we designed and fabricated wedges using the SRR-wire-post elements shown in Figure 17 (d, e, f, and g). We applied point group theory to these SRRs yielding Maxwell's equations shown in 2.4.5.7, to 2.4.5.12 describing the wedge media fabricated with the single- and balanced-SRRs. Equations 2.4.5.7 to 2.4.5.10 describe the bi-anisotropy of the single-SRR. Most of the equations for the single-SRRs have coupled E- and H-field only eq. 2.4.5.10 has a single H-field term. For the balanced-SRR wedge media equations 2.4.5.11 and 2.4.5.12 describe both balanced SRRs f and g in Figure 17. Equations 2.4.5.9 and 2.4.5.10 are the standard set of Maxwell's equations with permittivity ε and permeability μ. The balanced-SRRs will behave like an anisotropic material.

$$\nabla \times H = -j\omega\varepsilon_{xx} E_x - j\omega\xi_{xy} H_y \qquad \text{eq.}(2.4.5.7)$$

$$\nabla \times E = j\mu\zeta_{yx} E_{xx} + j\omega\mu_{yy} H_y \qquad \text{eq.}(2.4.5.8)$$

$$\nabla \times H = -j\omega\varepsilon_{xx} E_x - j\omega\xi_{zy} H_y \qquad \text{eq.}(2.4.5.9)$$

$$\nabla \times E = j\omega\mu_{yy} H_y \qquad \text{eq.}(2.4.5.10)$$

$$\nabla \times H = -j\omega\varepsilon_{xx} E_x \qquad \text{eq.}(2.4.5.11)$$

$$\nabla \times E = j\omega\mu_{yy} H_y \qquad \text{eq.}(2.4.5.12)$$

The wedges fabricated form the single- and balanced-SRR-wire-post were characterized[33], the

same way as our pervious nested-SRR-wire-post wedge, measuring the frequency response and angular beam pattern of the wedges. The measured frequency response and refractive index for the wedges are shown in Figure 39 (a, b, c, and d).

Figure 39 (a) shows the frequency response and refractive index for the single-SRR-wire-post wedge medium where only the H-field of the propagating wave excites the SRR resonance. Negative refraction occurred between 13 and 15 GHz and n is between -1.6 and 0 for the wedge. Positive refraction occurred between 15 and 18 GHz and n is between 0 and 1 for the wedge. The transition between the negative and positive refractive index was almost continuous. Figure 39 (b) shows the frequency response for the single-SRR-wire-post when both the E- and H-fields excite the resonance in the SRR. As seen in Figure 39 (b) the transmitted radiation passing thru the wedge was attenuated to the level of the noise floor of our measurement system. Since the transmitted power was so highly attenuated, the refractive index for the wedges could not be determined.

The dimensions of the balanced-SRRs in the media measured in Fig 39 (c) and (d) are exactly the same size as the single-SRR in the medium measured in Fig. 39 (a) and (b). The large shift in resonant frequency for balanced-SRRs is due the increase in capacitance between the parallel rings. The frequency range over which negative refraction occurs in for Figure 39 c and d is approximately the same 9 to 10.5 GHz, but there is a 230 MHz difference in frequency where n = -1 for c and d. In Fig. 39 (c and d) is the frequencies range over which n = 0 is different for Figure 39 (c) n = 0 is between 10.4 and 10.7 GHz approximately 300MHz while for Figure 39 (d) n = 0 is between 10.5 and 13.5 GHz approximately 3GHz. The frequency range over which n = 0 represents a stop band between the NRI and PRI. The PRI regions in Figure 39 (c and d) are different as well. The PRI region for Figure 39 (c) is between 10.8 to 12.3 GHz, but PRI region in Fig. 39 (b) starts at 13.5 GHz and continues to the upper frequency limit for the measurement setup at 18 GHz. These differences in Figure 39 (c and d) show that the orientations of the SRR gaps to the electric field of the propagating wave affect the properties of the media whether the media is bi-anisotropic or anisotropic.
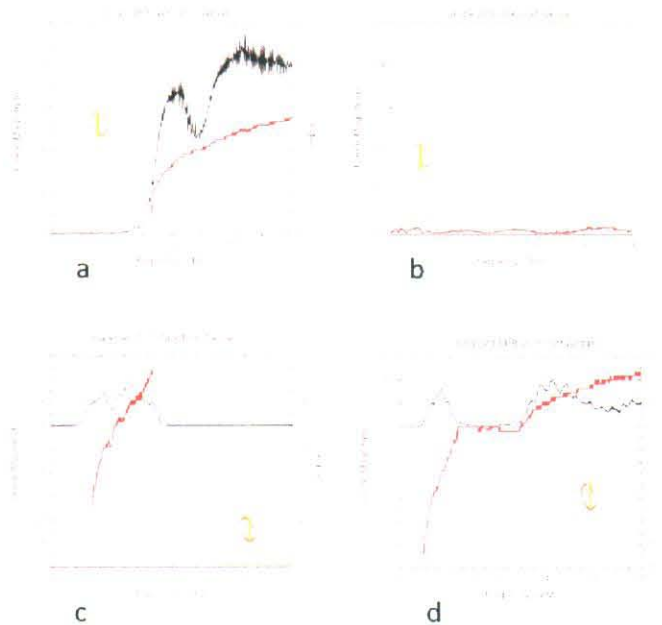

a   b

c   d

Figure 39: a, b, c, and d show the frequency response and refractive index as a function of frequency for the single- and balanced-SRR-wire-post wedge media.

2.5 Near Zero Refractive Index

The dispersion is easily seen in Figure 39 for SRR-wire-post media whether or not it is bi-anisotropic or anisotropic. In Figure 39(d) the refractive index shows a large range in frequency where n = 0. Since the n is defined as c/v_p where c is the speed of light in a vacuum and v_p is the phase velocity of the wave it is clear that as v_p approaches infinity as n approaches zero. It was proposed using Snell's law that a radiating source placed in an n = 0 medium would refract the radiation normal to the interface of such a medium n = 0. The concept is shown in Figure 40 where the dashed lines shows the refractive behavior for a source in a positive refractive index medium and the solid lines show the case where the source is in a n = 0 medium. This would be a useful property because we would be able to easily collimate our sources by placing them in such a medium. It would also mean that there would be no divergence of the source beam. There is one other physical implication of $v_p = \infty$ at n = 0. The phase would be the same anywhere in space in this medium. Since n = 0 is not really practical, we wanted to look at n → 0.
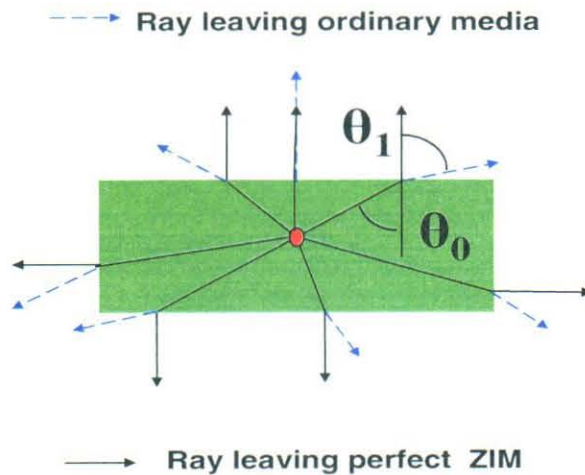
Figure 40: show a dipole source (red) embedded in a medium where the dashed rays indicate the refractive behavior of the source in a positive index medium and the solid rays indicate the refractive behavior for the dipole source in a zero index medium (ZIM) predicted by Snell's law.

We inserted a dipole into a slab fabricated with nested-SRR-wire-post element. The dipole antenna and slab are shown in Figure 41. The dipole antenna was characterized in air, then in the slab, and then in the slab with a reflector on one side of the slab[34].
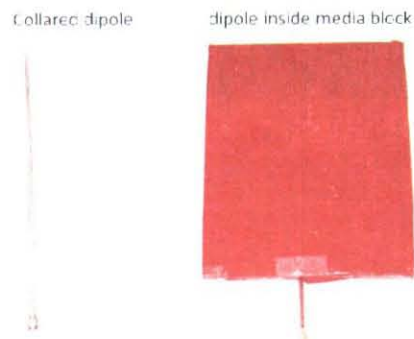
Figure 41: Shows the collard dipole and the nested-SRR-wire-post slab with the antenna inserted in it. The return loss for the dipole was less than 10 dB whether or not the dipole was in air or the slab.
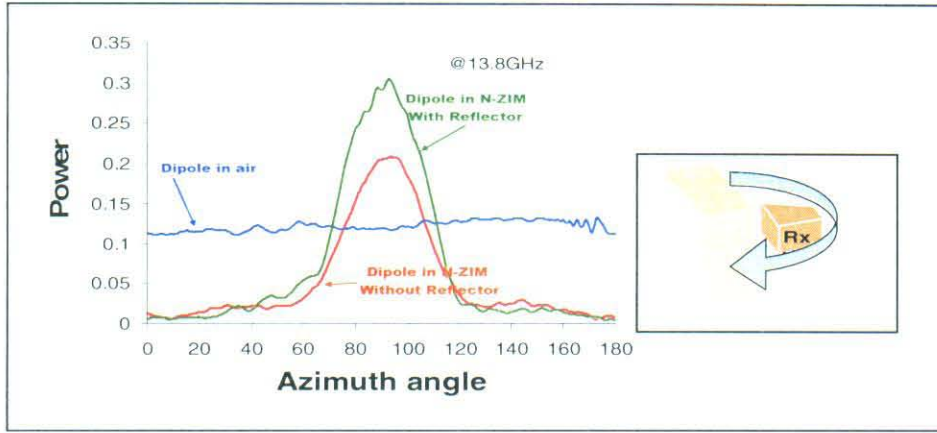
Figure 42: show a single axis measurement of the dipole in air and in the slab with and without a reflector placed on the 25 cm x 20 cm sides of the slab.

Figure 42 shows the results of the measurements for the dipole antenna and the antenna placed in the slab medium. The results show the omni-directional radiation pattern for the dipole antenna in air, the forward focused radiation pattern for the dipole antenna in the slab, and the increase forward power when a reflector was placed at the back surface of the slab medium. The measurements were made at 13.8 GHz where n = -0.5 in the medium. Since the behavior of the medium as n → 0 will be similar whether 0 is approached from positive or negative n, the choice of n = -0.5 was used because the best impedance (Z) match for the antenna in the slab medium was at 13.8 GHz. The radiation pattern for the slab with the dipole in indicates that no radiation was coming out of the sides of the medium. This is consistent with the asymmetry of the medium and the forward focusing of the radiation pattern. The half-power beamwidth (HPBW) of the radiation pattern was 27.5° which is inconsistent with a 10 λ width for the aperture of the slab (20 cm x 25 cm). To determine the optimal aperture size for the 27.5° HPBW, the analysis for the HPBW of a rectangular aperture with a uniform distribution[35] was used. The equation for a rectangular aperture is given in eq. 2.5.1, where Θ_{3dB} is HPBW, λ is the wavelength, L is the aperture length, and 0.89 radians is optimum Θ_{3dB} angle for a uniform rectangle. The aperture length was determined to be L = 40.2 mm for our $\Theta_{3dB} = 27.5°$ and λ = 21.7 mm.

$$\theta_{3dB} \approx \frac{0.89\lambda}{L}$$ eq. (2.5.1)

To determine effective aperture length of the metamaterial slab, a near-field scan was performed on the 16-cell thick slab with the source antenna inside. The slab was rastered in 1mm steps at 13.8 GHz, 10 mm above the surface. The result of the measurement is shown in the Figure 43. The half-power points for the near-field pattern approximately occupy a 40 mm x 40 mm area in the active region of the pattern. The results of the study for a near zero index metamaterial show that a source inserted in the near zero metamaterial can focus the power from an omni-directional source.
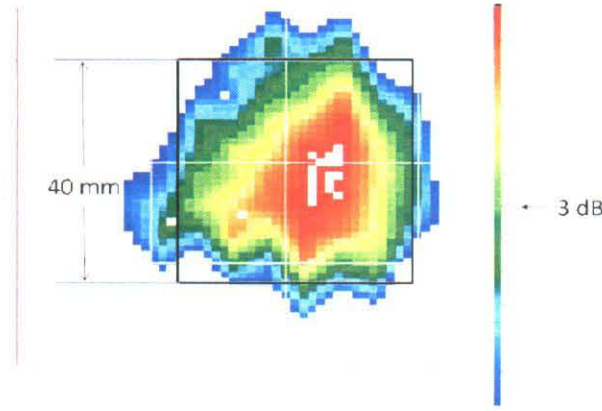
33

Figure 43 : near field measurements for the dipole driven for a16-cell thick slab medium rastered in 1 mm steps, 10 mm from the slab surface at 13.8 GHz. The rectangle in the figure outlines area of the beam within the 3 dB points.

2.6 Modulated Signals in Metamaterials

Most of the work on metamaterials particularly negative refractive index media has used CW plane waves. We collaborated with Steve Best and Drayton Hanna to study modulated signals thru a NIM medium[36,37]. The diagram for the electronics used to make the measurements is shown in Figure 44. The device under test used was placed in the baffle mounted on the rotation table in the anechoic chamber shown in Figure 22. The measurements were done by encoding a digital signal on a carrier frequency in the NRI bandwidth of wedge medium under test. The wedge makes it easier to isolate the negative refractive behavior by exaggerating the angle of refraction.
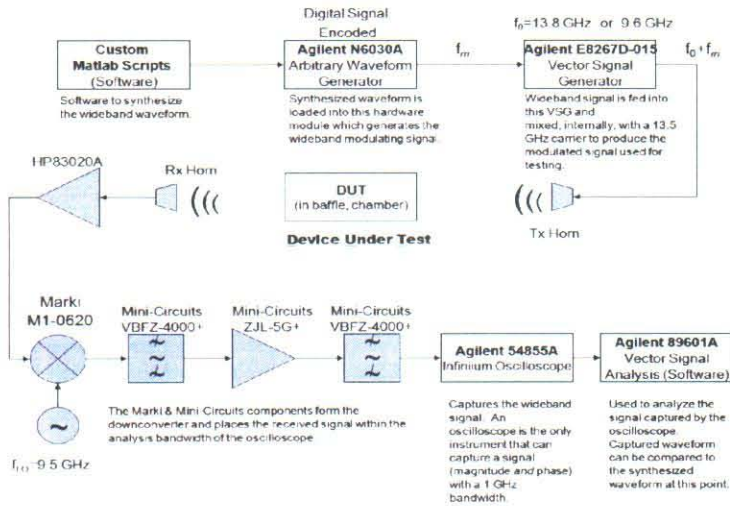
Figure 44: block diagram for QPSK measurement setup where the device-under-test (DUT) was a SRR-wire-post wedge.

Quadrature Phase Shift Keying (QPSK) was used to modulate the signal to measure the information bandwidth of the NRI medium. QPSK digital information was encoded on the carrier frequency to measure the effect of the frequency dispersion of the wedge on the modulated signal. The encoded signal was transmitted thru the wedge and the error in the encoded signal was measured upon reception after the signal was decoded. The bandwidth of the information encoded on the carrier signal was 400 MHz, and 800 MHz. Measurements were made with either a 13.8 or 9.6 GHz encoded with either the 400 or 800 MHz digital signal thru the open baffle in the anechoic chamber

34

to provide a base line reference for the measurement system in Figure 22 and 44. The results of the open baffle measurement for the 400 MHz modulation bandwidth on a 13.8GHz carrier is shown in Figure 45. Figure 45 consists of a constellation diagram, an eye diagram, and table of statistics where Error Vector Magnitude (EVM) is found. The constellation diagram shows the valid location of the magnitude and phase relative to the carrier frequency. There are 4 white circles that form a square and are the valid location for the magnitude and phase points on the constellation diagram. An ideal constellation diagram is symmetric about origin with the points filling the white circle at each corner forming a square. The constellation diagram in Figure 45 shows some error for the open baffle at 400MHz. The shape of the eye diagram provides information about timing errors, signal excursion, the amount of sampling distortion over the time at which the waveform is successfully sampled, and the best sampling time. The EVM is the bit rate error in the decoded signal for the open baffle, the EVM was 8.5%.

Constellation Diagram   Eye-diagram   EVM Statistics
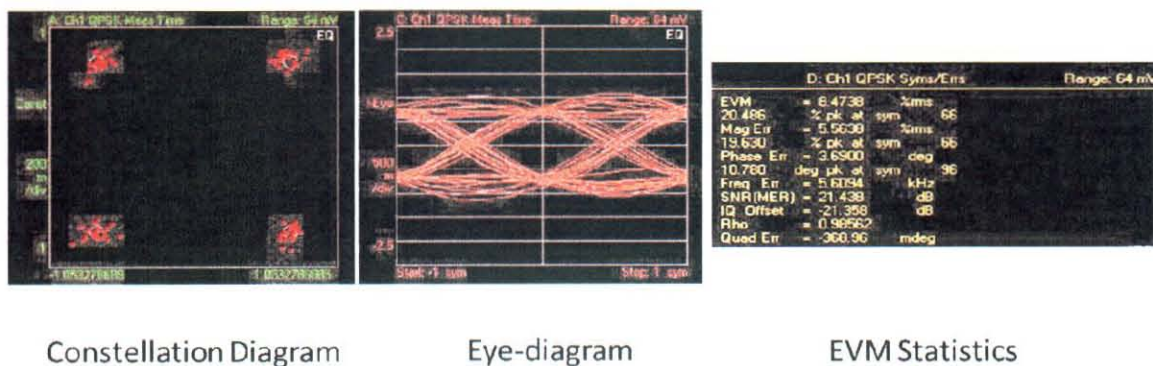
Figure 45: Constellation diagram, eye diagram, and EVM for the open baffle for a carrier frequency of 13.8GHz and a 400MHz modulation.

The 13.8 GHz carrier frequency was used to measure the information bandwidth of the nested-SRR-wire-post wedge. Figure 46 shows the constellation and eye diagram and EVM as a function of frequency results for the 400MHz modulation bandwidth. The symmetry in the constellation diagram shows a number of scattered points around the white circles at the corners of the square. The eye diagram shows little or no change compared to the eye diagram for the open baffle. The EVM in the statistics is 12.1% approximately a 4% increase compared with the open baffle.

Constellation Diagram   Eye-diagram   EVM Statistics

Figure 46: Constellation diagram, eye diagram, and EVM for the nested-SRR-wire-post wedge with a 13.8GHz carrier frequency and a 400MHz modulation.

35

Figure 47 shows the measurement result for the open baffle at 800MHz. The constellation diagram shows the points around the white circles are spread out, but still form the shape of a square and the EVM is 8.5%. The measurement results for the wedge at 800MHz are shown in Figure 48. It is easily seen the widely distributed points in the constellation pattern do not form a square. The eye diagram does not resemble an open eye and the rms EVM is in excess of 50%. This result for nested SRR wedge was expected since its NRI bandwidth is approximately 650 MHz and the bandwidth of the modulated signal is 800MHz.

Constellation Diagram   Eye-Diagram   EVM Statistics

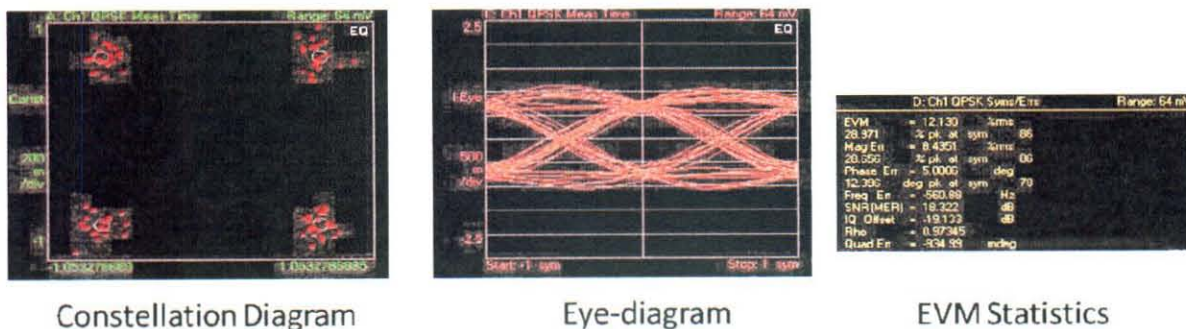**Figure 47: Constellation diagram, eye diagram, and EVM for the open baffle with a 13.8GHz carrier frequency and a 800MHz modulation**

Constellation   Eye-diagram   EVM Statistics

Figure 48: Constellation diagram, eye diagram, and EVM for the nested-SRR-wire-post wedge with a 13.8GHz carrier frequency and a 800MHz modulation.

A balanced-SRR-wire-post wedge was also characterized. A 9.6GHz carrier frequency was used for the balanced-SRR-wire-post wedge. The balanced-SRR-wire-post wedge was measured with a 400 and 800 MHz modulation signal the same as the nested-SRR-wire-post wedge. Figure 49 and 50 show the measurement results at 400 MHz for the open baffle and wedge respectively. The constellation diagram shows the points are highly clustered around the white circles forming a well defined square for the open baffle. The points in the constellation diagram for the wedge shows some spreading around the white circles, but still show a highly defined square for the balanced-SRR wedge. The eye diagram for both the open baffle and wedge show a well defined line shape and a large eye opening. The measured EVM for the open baffle EVM was 4.96% balanced-SRR wedge was 9.46%, a the difference of approximately 4.5%.

Constellation Diagram   Eye-Diagram   EVM Statistics

Figure 49: Constellation diagram, eye diagram, and EVM for the open baffle with a 9.6GHz carrier and a 400MHz modulation frequency.

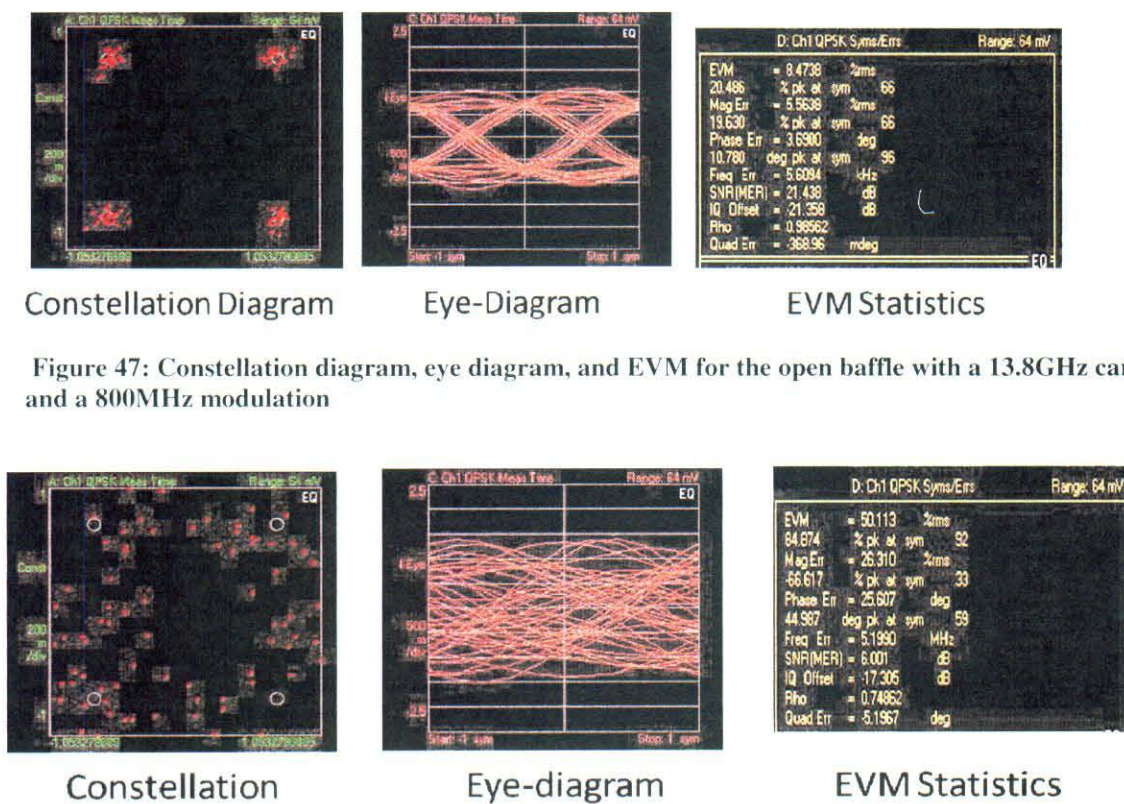Constellation Diagram   Eye-Diagram   EVM Statistics

Figure 50: Constellation diagram, eye diagram, and EVM for the balanced-SRR-wire-post wedge with a 9.6GHz carrier and a 400MHz modulation frequency

The 800 MHz modulation bandwidth measurements for the open baffle and balanced-SRR wedge are shown in Figure 51 and 52 respectively. The constellation pattern for balanced-SRR wedge at 800 MHz is noisy compared to the open baffle, but has enough of a square symmetry to decode the signal. The eye diagram shows increased spreading in the line shape, but still maintains its eye shaped pattern even though it is with a much narrower eye opening. The EVM for the wedge was 23.33% and 6.91% for the open baffle at 800 MHz, approximately a 16% difference between the wedge and open baffle.

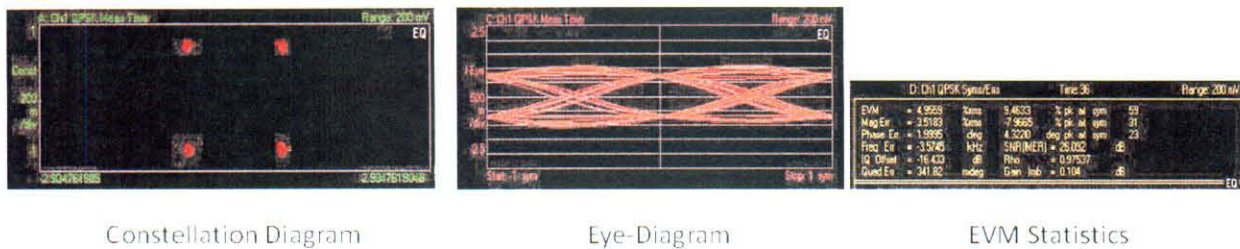Constellation Diagram   Eye-diagram   EVM Statistics

Figure 51: Constellation diagram, eye diagram, and EVM for the open baffle with a 9.6GHz carrier and a 800MHz modulation frequency

37
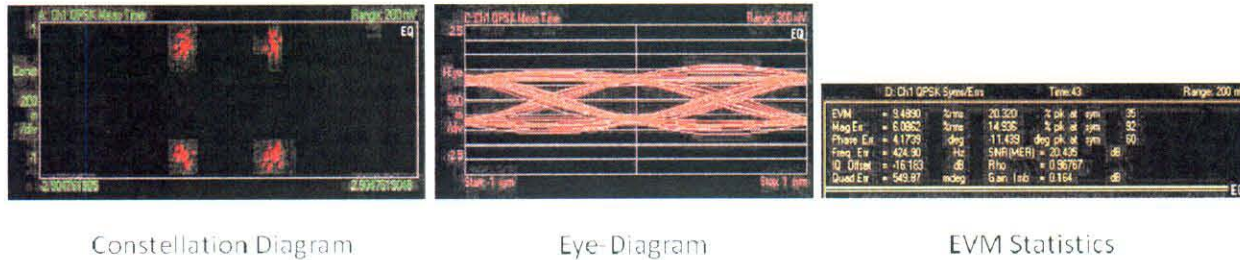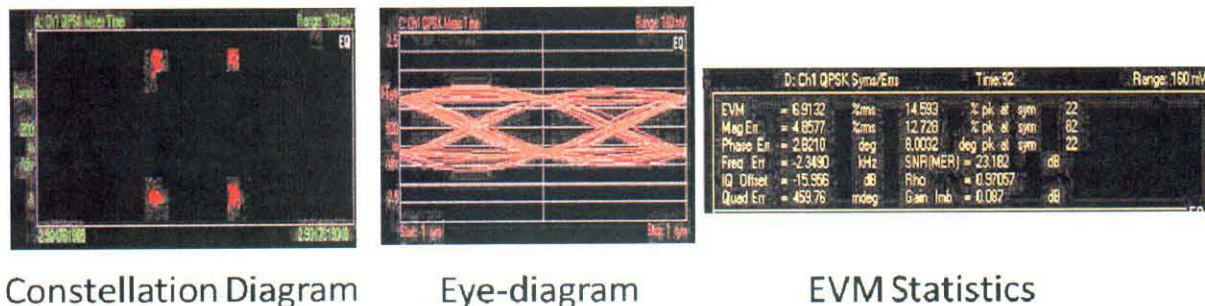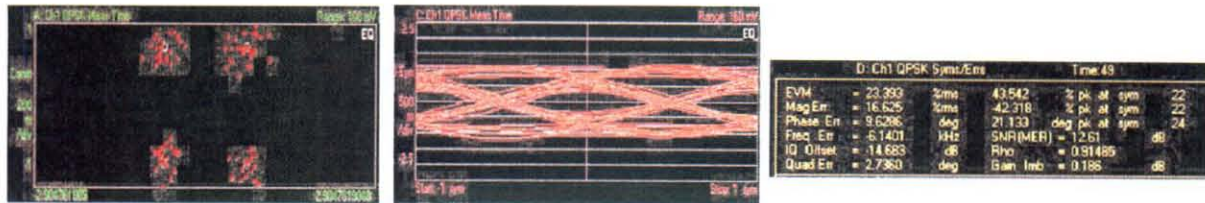
| Constellation Diagram | Eye-Diagram | EVM Statistics |

Figure 52: Constellation diagram, eye diagram, and EVM for the balanced-SRR-wire-post wedge with a 9.6GHz carrier and a 800MHz modulation frequency

The result for the balanced-SRR wedge at 800 MHz is understandable since the NRI bandwidth of the balanced wedge is 800MHz. Two notable comments about the measurements are 1) the 800 MHz modulation frequency was the maximum modulation bandwidth for the measurement setup and 2) neither of the nested-SRR- or balanced-SRR-wire-post wedges were optimized for bandwidth or loss. Since the operational bandwidth of the balanced-SRR wedge was not exceeded, it does show that NIM can be used in applications where modulated signals are within the NRI bandwidth.

3.0 SURFACE PLASMONS

3.1 Introduction

A plasmon is commonly defined as a collection of highly mobile electrons and ions that forms a neutral gas (e. g. the ionosphere). Metallic solids, with a high density of electrons, in their conduction bands or semiconductors with relatively high densities of carriers (electrons and holes) in both their valence and conduction bands can be modeled as a plasma under certain conditions. Plasmas not only exist in the volume of solids, but can also exist at the solid/ambient interfaces and the surface of the solid. The surface charge density forms small dipoles which can propagate a longitudinal wave which run along the surface and penetrate into a solid and into the adjacent atmosphere. The longitudinal waves are referred to as surface plasmons[38]. Recently surface plasmon interactions have been used to demonstrate optical devices such as sensors and readouts[39,40]. The properties of plasmons allow its wavelength to be much smaller than the free space wavelength at the same frequency. The smaller wavelength can enable optical components below the Rayleigh limit of ordinary optical components. This could have ramifications in the size and speed of integrated optical components and devices.
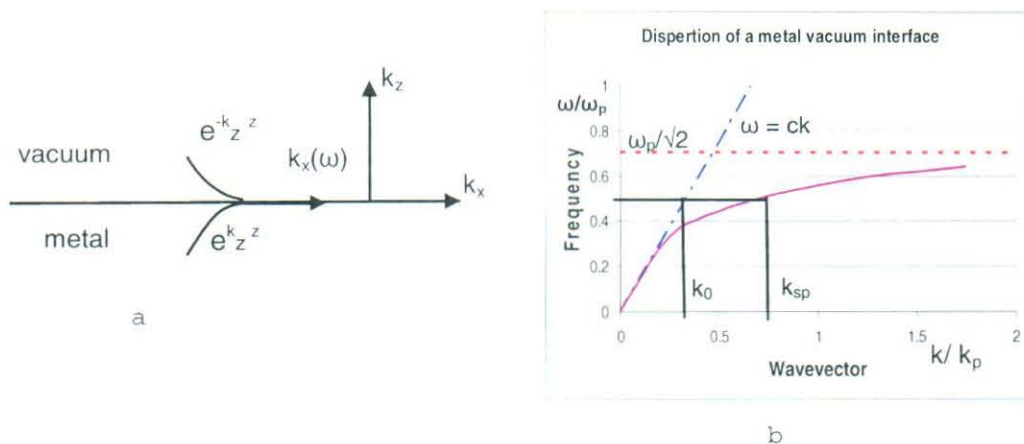
The diagram in Figure 53 (a) shows the longitudinal surface plasmon wave propagating along a metal surface and the exponential decay of the surface wave in both media at the interface. Form Figure 53 (b) shows the dispersion for light and the surface plasmon in the metal. From the dispersion diagram it can be seen that the momentum of the surface plasmon wave and light wave is highly mismatched, indicating an ordinary light wave incident on the surface of the medium will not excite the surface plasmon.

3.2 Coupling to a Surface Plasmon

3.2.1 Grating and Nano-hole Coupler
To match the momentum of the surface plasmon to the light wave two most common techniques are the use of gratings or prisms. Figure 54 shows cross sectional view of a grating and an array of nano-holes in a metal film..
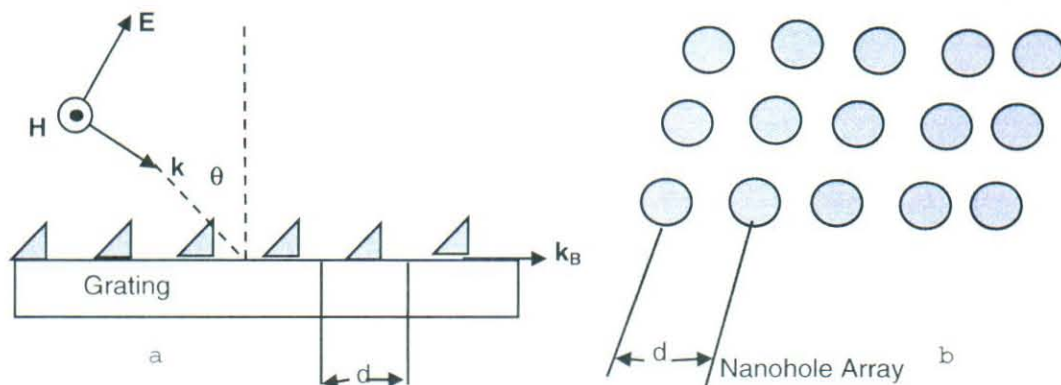

Figure 54: (a) is a cross sectional diagram of a metal grating with period d and a TEM wave incident on surface (b) is a square array of nano-holes in a metal film, or metallic nano-dots on a dielectric film, that can be used as a grating with period d.

Figure 54(a) shows a transverse electromagnetic wave (TEM) incident on the grating at an angle θ relative to the normal of the grating. The vector k_B is the projected component of the wave vector incident on the grating. The periodic surface of the grating can exchange momentum with the surface plasmon. The momentum exchange by the grating surface is given by $\pm 2\pi n/d$ where n is an integer and d is the period of grating. For a given surface plasmon wave vector $k_{SP} = k_B \pm 2\pi n/d$[23]. The array of nano-holes in the thin metal film in Figure 54(b) works the same way as the grating. The momentum exchange for the array of nano-holes is given by $\pm 2\pi n/d$ where n is an integer and d is period of the holes. Since the wave vector on the surface of the grating or the array of holes is the projection of the incident TEM wave vector, the excitation of the surface plasmon resonance will have an angular dependence with respect to the incident light direction.

3.2.2 Prism Coupler
The prism coupler[41] shown in Figure 55 (a) can excite a surface plasmon resonance in the metal. Figure 55 (a) shows a prism-spacer-metal configuration. The prism is used to excite the surface plasmon resonance by total-internal-reflection at the prism-spacer interface. Total-internal-reflection is achieved when the refractive index of the spacer is less than the refractive index of the

prism like a glass-air interface. Total-internal-reflection occurs when light incident at the prism-spacer interface is greater than or equal to a critical angle α. When total-internal-reflection occurs an evanescent surface wave is produced at the prism-spacer (air) interface. The evanescent surface wave can then couple to the electric-dipole moments to drive the surface plasmon resonance. Since the surface plasmon resonance generates a longitudinal propagating wave, the evanescent surface wave at the prism-air needs a longitudinal electric-field component. A transverse magnetic (TM) evanescent surface wave can be produced at the prism-air interface. The TM wave has a longitudinal electric-field component and is produced when linearly polarized light is parallel to the plane of incidence (p-polarized) at prism-air interface. When the evanescent TM wave couples to the plasmon resonance the intensity of the reflected light is attenuated.
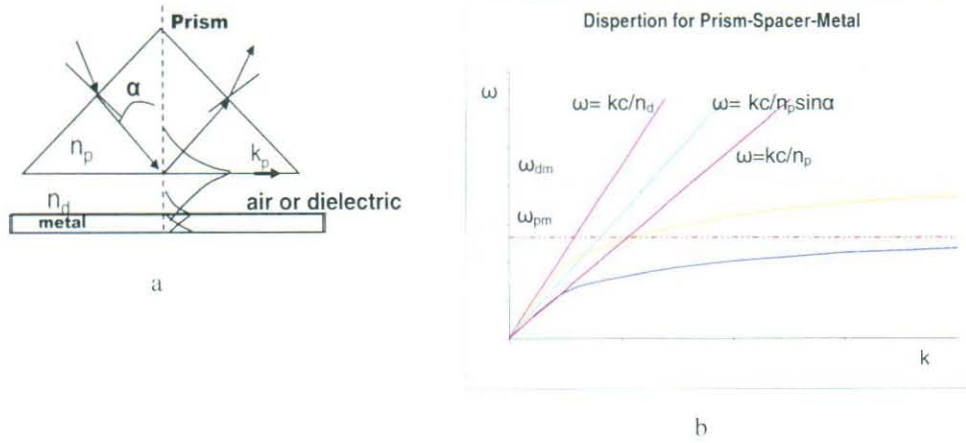

Figure 55: (a) A diagram of a prism-spacer-metal configuration and 55(b) shows the dispersion relationships for light, light in the prism and the surface plasmon dispersion for a metal-air interface(dm) and, in the limit where the goes to zero, a metal-prism interface(pm).

Figure 55 (b) shows the associated dispersion curves for light in air, light in the prism, an air-metal interface, and a prism-metal interface. The dispersion of the prism-metal asymptotically approaches $\frac{\omega_{pm}}{\sqrt{2}}$ where ω_{pm} is the plasma frequency for the prism-metal interface. The dispersion curve for light, in the prism is $\omega = \frac{kc}{n_p}$ where k is the wave vector, c is the speed of light in vacuum, and n_p is the refractive index of the prism. The light line for air for in the plot is $\omega = \frac{kc}{n_d}$ where n_d is the refractive index for air and the dispersion curve for air-metal interface asymptotically approaches $\frac{\omega_{dm}}{\sqrt{2}}$ where ω_{dm} is the plasma frequency for the air-metal. In Figure 55 (b) it can be seen that the light line in the prism does not intersect the prism-metal dispersion curve nor does light line for air intersect the air-metal dispersion curve. The dispersion relationship for the light line in prism-air-metal configuration is bound by the air-light line at the upper bound and prism-light line at the lower bound. The light line for the evanescent wave is given by $\omega = kc \sin \alpha / n_p$ where α is an angle equal to or greater than the critical angle for total internal reflection. In Figure 55 (b) the light-line for the evanescent wave intersects the plasmon dispersion curve for the air-metal interface. At this intersection point the momentum of the evanescent wave and the surface plasmon match driving the resonance of the surface plasmon. By changing the angle α the light-line moves between the bounds of the light-lines for air and the

40

prism. As α changes the light-line for the evanescent wave, it will intersect different points along air-metal dispersion curve allowing the wave to couple with the plasmon resonance at those frequencies.

Since the plasmon resonance requires a longitudinal electric field to couple to its electric dipole moment, the plasmon interaction can be verified by changing the polarization of the light. A transverse electric (TE) evanescent surface wave can be produced at prism-air interface. The TE wave has a longitudinal magnetic-field component. TE wave is produced when polarized light perpendicular to the plane of incidence (s-polarized) at prism-air interface. The TE surface wave will not excite a surface plasmon resonance in the metal and therefore no attenuation will be evident in the reflected light.

3.3 Optical NIM

The initial demonstration of a NIM came from Sir John Pendry's conceptual designs[17,25] for producing $\varepsilon < 0$ and $\mu < 0$. Pendry's wire grid structure simulated behavior of a plasmon to produce an $\varepsilon < 0$ and his SRRs simulated a ferromagnetic resonance behavior to produce $\mu < 0$ at microwave frequencies.

Since plasmons exist at optical frequencies, the problems is finding a structure at optical frequencies to produces $\mu < 0$ like the SRRs since SRRs do not scale to optical frequencies. NIM media at optical frequencies will provide the material for fabricating optical and or electro-optical components and devices that do not presently exist, but are wanted for applications like electronic beam steering at optical frequencies. Nano-size particles like dots, spheres, rods, etc... have been proposed in the literature[42] NIM material composites use nano-size conductors in a dielectric or semiconductor medium. The problem with validating the proposed nano-structure and making make an optical NIM is controlling the size and placement of the nano-particles during fabrication. One of the simplest nano-size particles are dots. The nano-dots can produce resonant electric and magnetic dipole moments to generate a negative ε and μ.

We are studying the electromagnetic behavior of nano-dots in single- and mutely- layer media for their plasmon and NRI behavior. We have constructed nano-dot media by means of random size and oriented gold colloidal dots layered between aluminum oxide films. These dots were made by depositing a gold film of a defined thickness on the sputtered layer of aluminum oxide. The thickness of the gold film allowed control of the average diameter of the dot. The gold film was then annealed between 500^0C and 600^0C causing the gold to coagulate into dots. Another layer of aluminum oxide was then deposited the over the nano-dots and gold processing was repeated. Up to four layers of nano-dots/alumina have been made this way thus far producing nano-dots that had between 500 nm and 70 nm for the given medium. Figure 56 shows SEM pictures after the annealing process. The nano-dots shown in A are the 500 nm dot medium and in B are the 70 nm dot medium after the annealing process.
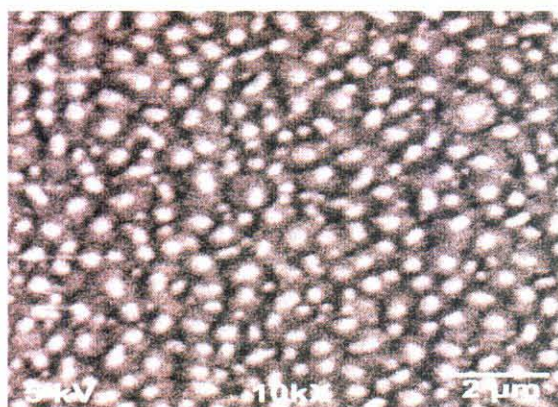
A
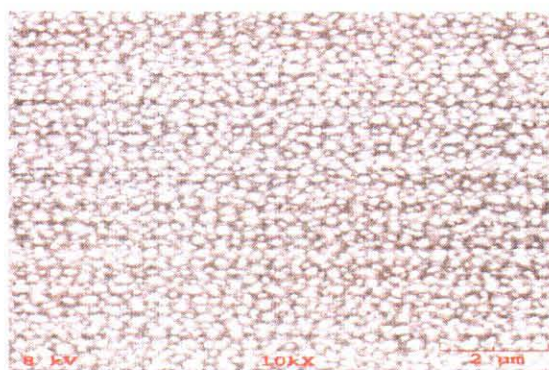
B

Figure 56: SEMs of gold nano-dots after annealing. Both images were taken at 10,000X and have a 2 micrometer reference line. 56A) 500nm dot medium, 56B) the 70nm dot medium

The transmittance of the 500nm dot and 70nm dot medium was measured from 200 to 2000nm and are shown in Figure 57. The 500nm dot medium shows a transmittance peak at approximately 450nm and a rate of change from 10 to 70 % in the transmittance between 1000 and 2000nm. The transmittance measured for the 70nm dot medium is shown in Figure 57B. The 450nm peak is visible for 70nm dot medium, in addition a second peak is observed at approximately 850nm. The second transmittance peak for the 70 nm medium is not immediately obvious. Since the dot size was reduced to 70 nm, one would expect to observe a change in transmittance at a shorter wavelength rather than a longer wavelength. Further work will be required to reconcile this non-intuitive behavior. The rest of the transmittance for the medium follows a similar pattern to that of the 500nm dot medium.

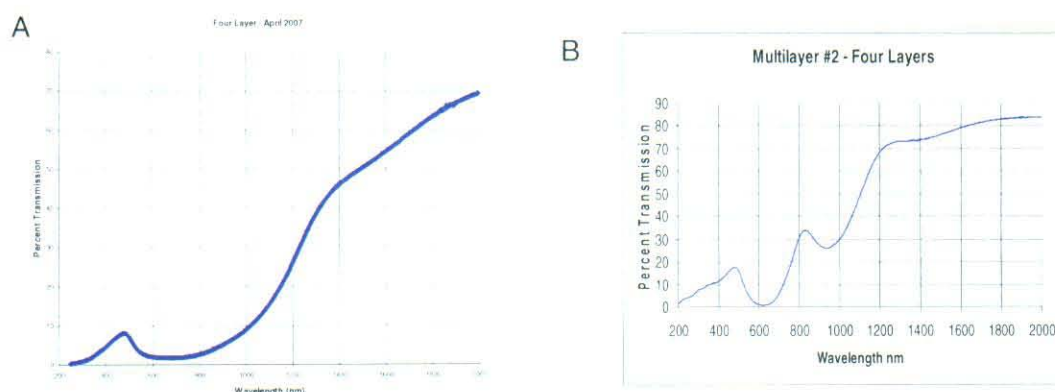Figure 57: A) Transmittance response for the 500nm nano-dot medium, B) the transmittance response for the 70nm nano-dot medium.

Mie scattering theory[44] predicates an electric dipole moment and a magnetic dipole moment for conducting spheres in a dielectric medium. Using s- and p- polarized light the different dipole moments could be addressed independently by measuring the reflectivity for the 70nm medium.

42

Our initial study of the reflectivity was performed at a wavelength of 633nm. Figure 58 shows the reflectivity for 70nm medium as a function of angle using the two polarizations of light. The line shape for p-polarized and s-polarized light both show minima in their reflectivity, but at different angles of incidence. Mie theory de-convolutes incident transverse electromagnetic wave (TEM) into a transverse electric (TE) and transverse magnetic (TM) waves for conducting spheres or particles in a dielectric medium. The TE and TM waves cause the local fields around the spheres to form the electric and magnetic dipole moment respectively, wherein the TM wave is associated with the electric dipole moment and the TE wave is associated with the magnetic dipole moment. The layers of the medium act like a grating which causes a Plasmon wave to be produced from p-polarized incident waves. The combined (quasi-) periodicity of the gold particles and the periodicity of the (four) layer construction creates a favorable condition for plasmon-like interaction of with either TE or TM waves. Thus, the incident s-polarized wave can produce a magnetic plasmon wave by interacting and coupling with the local fields of the particle's magnetic dipole moments.
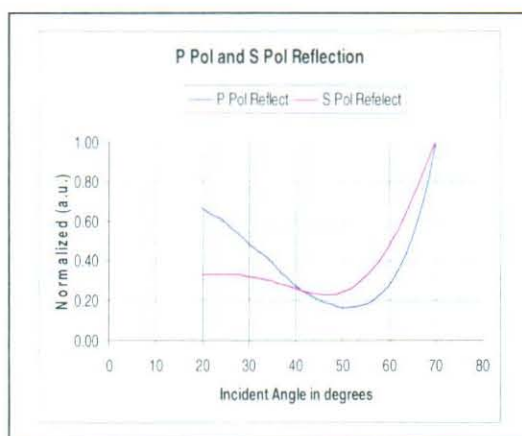
Figure 58: Reflectivity response of the 70nm medium for s- and p-polarized (633nm source).

The added ability to acquire information for the local TE and TM waves of the nano-dots is an important point. Since negative refractive index media requires both an electric dipole moment and magnetic dipole moment, a negative refractive index media would be facilitated if both moments of equal momentum can be created in the same nano-particle medium. Work is continuing to understand how to control the behavior of the electric and magnetic dipole moments of this medium and other nano-structures like spheres or cylinders for resonant structures to provide a $\mu < 0$ at optical frequencies.

REFERENCES

1. J. G. Bednorz and K. A. Muller,"Possible High Tc superconductivity in the Ba-La-Cu-O system", Z. Phys. B, Vol. 64, pp.. 189-193, June 1986.

2. K. M. Wu, et al., "Superconductivity at 93 K in a new mixed-phase Y-Ba-Cu-O compound system at ambient pressure", Phys. Rev. Lett. Vol. 58, Issue 908, 1987.

3. R. J. Cava et al, "Bulk Superconductors a 91 K in Single-Phase Oxygen-Deficient Pervoskite $Ba_2YCu_3O_{9-\delta}$," Phys Rev Lett Vol. 58, No. 16, pp1676-1679, 1987

4. D. E. Oates, S.-H. Park, D. Agassi, and K. Koren, Supercond, Sci. Technol., 17, S290 (2004)

5. Balam A. Wilemsen, J. S. Derov, S. Sridhar, "Critical-state flux penetration and linear microwave vortex response in $YBa_2Cu_3O_{7-\delta}$," Phys. Rev B, Vol. 56, No. 18, Nov. 1997, pp. 989-996

6. G. Hammerl, A. Schmehl, R. R. Schultz, B. Goetz, H. Bielefeldt, C. W. Schmeider, H. Hilgenkamp, and J. Mannhart, Nature, 407,162 (2000)

7. S. Seron, D. E. Oates, G. Hammerl, J. Mannhart, P. J. Hirst, R. G. Humphreys, A. C. Anderson, M. A. Hein, and J. Derov, "linear and Nonlinear Microwave Properties of $YBa_2Cu_3O_{7-\delta}$ Thin Films", Phys. Rev. B, 72, 104511 (2005)

8. G. L. Skofronick, A. H. Camrin, S.R. Feltyn, and R. E. Muenchausen, J. Mater. Res. 8, 2785 (1993)

9. J. Moreland, P. Rice, S. E. Russek, B. Jeanneret, A. Roshko, R. H. Ono, and D. A. Rudman, Appl. Phys. lett., 59, 3091 (1991)

10. E. A. Giess, R. L. Sandstorm, W. J. Gallagher, A. Gupta, S. L. Shinde, R. F. Cook, E. I. Cooper, E. J. M. O'Sullivan, J. M Roland, A. P. Segmuller, and J. Angiello, IBM J. Res. Dev. 34, 916 (1990)

11. B. Crossely, J. R. Reid, J. S. Derov, E.E. Crisman, A. Corrales,A. J. Drehman and J. R. Reid "Surface Etching of YBCO Films by Xenon Difluoride," Vazuum Science and Technology B23, 1607 (2005).

12. C. Goldsmith, J. Randall, S. Eshelman, and T. H. Lin, "Characteristics of micro-machined switches at microwave frequencies," IEEE Microwave Theory and Techniques Symposium, pp. 1141-1144, March 1995

13. V. G. Veselago, "The Electromagnetics of Substances with Simultaneously Negative Values of ε and μ", Soviet Physics USPEK, Vol. 10, No. 4, p. 509, Jan-Feb 1968

14. N. W. Ashcroft and N. D. Mermin, "Solid State Physics," Sanders College, 1976, Chap. 1

15. J. B. Pendry, A. J. Holden, W. J. Stewart, and I. Young, "Extremely Low Frequency Plasmons in Metallic Mesostructures", Phys. Rev. Lett., Vol 76, No. 25, pp. 4773-4776, 17 June 1996

16. J. B. Pendry, A. J. Holden, D. J. Robins, and W. J. Stewart, "Magnetism from Conductors and Enhanced Nonlinear Phenomena", IEEE Trans. MTT. Vol. 47, No. 11, pp. 2075-2084, Nov. 1999

17. D. R. Smith, Willie J. Padilla, D. C. Vier, S. C. Nemat-Nasser, and S. Shcultz, "Composite Medium with Simultaneously Negative Permeability and Permittivity", Phys. Rev. Lett., Vol. 84, No. 18, May 2000, pp 4184-418

18. Said Zouhdi et al, eds., Advances in Electromagnetics of Complex Media and Metamaterials, Kiuwer Academic Publishers, 2002, pp 99-121

19. D.R. Smith and J. B. Pendry, "Homogenization of metamaterials by field averaging," J. Opt. Soc. Am. B, Vol. 23, No. 31, March 2006, pg 391

20. Th. Koschny, P. Markos, E. N. Economou, D. R. Smith, D. C. Vier and C. M. Soukoulis, "Impact of inherent periodic structures on effective medium descriotion of left-handed and Related metamaterials," Phys. Rev. B 71, 245105, 2005

21. Claudio G. Parazzoli, Robert B. Greegor, Minas H. Tanielian, David R.Smith, Steve Cummer, David Schurig and Richard Ziolkowski, "Applications of Metamaterials in the GHz Frequency Domain," Proc. IEEE Antennas and Propagation Society International Symposium,Honolulu, Hawaii, June 2007

22. W.J. Padilla, D. R. Smith and D. N. Basov, "Spectroscopy of metamaterials from infrared to optical frequencies," J. Opt. Soc. Am. B, Vol. 23, No. 31, March 2006, pg 404

23. E. Narimanov, B. L. Sivco and C. Gmachl, "Negative refraction in semiconductor metamaterials," Nature Published Online 14 October 2007, www.nature.com/naturematerials

24. A. Geria,Kussow, A. Akyurtlu, A. Semichaevsky and N. Angkawisittipan, "MgB_2 –based negative refraction index metamaterials at visible frequencies: Theoretical analysis," Phys. Rev. B 76, 195123 2007

25. R. A. Shelby, D. R. Smith, and S. Schultz, "Experimental verification of negative index of refraction," Science, Vol. 292, pp. 77-79, 2001

26. J. S. Derov, B. W. Turchinetz, E. E. Crisman, A. J. Drehman, A. R. Best and R. M. Wing, "Free space Measurements of Negative Refraction With Varying Angles of Incidence," IEEE Microwave and Wireless Components Letters, Vol. 15, No. 9, Sept. 2005 pg. 567

27. A. M. Nickolson and G. F. Ross, "Measurements of the Intrinsic Properties of Materials by Time Domain Techniques," IEEE Trans. Instrum. Meas., Vol. IM-19, Nov. 1970, pp. 377-382

28. J. Derov, B. Turchinetz, E. Crisman, A Drehman, and S.Best, "The microwave behavior of an anisotropic negative index medium," Proc. SPIE Vol. 6003, 600300-1, 2005

29. R. Marques, F. Medina and R. Rafii-El-Idrissi, "Role of bianisotropy in negative permeability and left-handed metamaterials," Phys. Rev. B, 65, 144440 2002

30. J. S. Derov, B. W. Turchinetz, E. E. Crisman, A. J. Drehman S. R. Best, "MEASURED POLARIZATION RESPONSE OF NEGATIVE INDEX METAMATERIAL", Proceedings 18th International Conference on Applied Electromagnetics and Communications (ICECom 2005), Dubrovnik, Croatia, 12-14 October 2005

31. N. Wongkasem, A. Akyurtlu, and K. M. Marx, "Group Theory Based Design of Isotropic Negative Refractive Index Metamaterials," PIER 63, 295-310, 2006

32 W. Padilla, "Group Theory Description of Artificial Metamaterials," Optics Express, Vol. 15, No. 4, pp. 1639-1646, 2007

33. J. S. Derov, B. W. Turchinetz, E. E. Crisman, and A. J. Drehman J. W. Dean, "Free Space Measured Loss Comparison of Single and Double Ring Resonators for Negative Index Media ," Proceedings, IEEE Antenna and Propagation Society International Symposium, 2008

34. B. W. Turchinetz, J. S. Derov, S. R. Best, E. E. Crisman, A. J. Drehman, J. P. Kenny and R. P. DiMasi, "Experimental Use of Metamaterials as an Antenna Collimator," Proc. of the Antenna Applications Symposium, ALLERTON Park Monticello, Ill. 21-23 Sept. 2005, pp 23-36

35. John D. Kraus, "Antennas," 2nd ed., McGraw-Hill, 1968, pg 847

36. D. L. Hanna, S. R. Best, B. W. Turchinetz, J. S. Derov, "Experimental Verification that a Metamaterial Wedge Supports the Propagation of a Bandlimited Modulated Signal," Proceedings, IEEE Antenna and Propagation Society International Symposium, 2008

37. Steve R. Best, Drayton Hanna, Beverly W. Turchinetz, John S. Derov, "Validation of Negative Refraction in a Metamaterial Wedge using QPSK Modulated Signals", Published in the Proceedings of iWAT2008, Chiba, Japan, March 2008

38. H. Raether, "Excitation of Plasmons and Interband Transition by Electrons", Springer-Verlag, 1980, Chap. 10

39. Stefan A. Maier and Harry A. Atwater, "Plasmonics: Localization and guiding of electromagnetic energy in metal/dielectric structure", J. Appl. Phys., 98, 01101, 2005

40. Harry A Atwater, "The Promise of Plasmonics", Scientific American, pp. 56-63, April, 2007

41. A. Otto, "Excitation of Non-Radiative Surface Plasma Waves in Silver by the Method of Frustrated Total Reflection", Z. Phys. 216, 398 (1968)
42. Andrea Alu and Nader Engheta, "Guided Modes in a Waveguide Filled With a Pair of Single-Negative (SNG), Double-Negative (DNG) and/or Double-Positive (DSP) Layers", IEEE Trans. MTT., Vol. 52, No. 1, pp. 199-206, Jan. 2004

43. Andrea Alu, Alessandro Salandrino, and Nader Engheta, "Negative effective permeability and left-handed materials at optical frequencies," Optics Express, Vol. 14, No. 4, pp. 1557-1564, 2006

44. Mie scatter M. Born and E.Wolf, "Principles of Optics", 5th ed., Pergamon Press, 1975, Chap. 13, pp. 634-656.